

Submesoscale current effects on surface waves

Leonel Romero ^{a,*}, Delphine Hypolite ^b, James C. McWilliams ^b



^a Earth Research Institute, University of California, Santa Barbara, United States of America

^b Department of Atmospheric and Oceanic Sciences and Institute of Geophysics and Planetary Physics, University of California, Los Angeles, United States of America

ARTICLE INFO

Keywords:

Wave-current interactions
Current effects on waves
Air-sea fluxes
Wave breaking

ABSTRACT

We present a numerical study of current effects on waves (CEW) at submesoscales (100's of m–10's of km) with a realistic model configuration in Southern California. CEW is analyzed by comparing solutions forced by winds with and without current forcing through relative differences. The modulation of wave field due to currents is larger for the wave-breaking variables (i.e., whitecap coverage, air-entrainment, and energy dissipation) followed by the resolved mean square slope, surface Stokes drift, and the significant wave height. Background currents on average increase the directional spreading by 0.9° and modulate the mean wave direction within ± 5°. CEW decreases with increasing wind speed because the rms current gradients also decrease while the wind forcing and breaking restore the wave field towards equilibrium faster at higher winds. Empirical scalings based on the mean wave period, rms current gradients, and friction velocity are found to explain 80% or more of the variability for the model differences due to CEW except for the significant wave height, explaining 66% of the variability. The statistics of model differences due to CEW are approximately Gaussian for the significant wave height, symmetric with finite excess kurtosis for the higher spectral moments, and positively skewed with excess kurtosis for the wave-breaking variables.

1. Introduction

Wave-current interactions can be divided into current-effects on waves (CEW) and wave effects on currents (WEC). This study is concerned with the former, in particular, the modulation of the wave field at submesoscales O(1 km or smaller). In recent years, CEW has gained interest in the literature due to its relevance for remote sensing, the modulation of wave breaking and related air-sea fluxes, and the incidence of extreme waves (Janssen and Herbers, 2009; Hjelmervik and Trulsen, 2009; Onorato et al., 2011). Moreover, CEW allows for the investigation of the wave spectrum modulation from wind-wave equilibrium (Phillips, 1984). Kudryavtsev et al. (2017) reported a novel characterization of the wave spectral variability due to currents inverting spectra from satellite sun-glitter imagery with supporting altimeter data. Ardhuin et al. (2017) used satellite altimetry and realistic models to show that the modulation of the wave field by currents at scales from 10's to 100's of kilometers is significant, with the significant wave height varying by more than 50% at scales of 10's of km. Quilfen et al. (2018) presented an analysis of the wave field across the Agulhas current with satellite altimeter and synthetic aperture radar (SAR), finding consistent patterns with a wave model forced with surface currents from altimeter but the impacts due to currents were under-predicted. The global analysis of satellite altimetry data by Quilfen and Chapron (2019) showed a clear relation

between the dominant mode of spatial variability of the wave field and that of the sea surface topography indicating a strong coupling of the wave field to ocean currents at mesoscales supporting the findings of Kudryavtsev et al. (2017) and Ardhuin et al. (2017).

Romero et al. (2017) reported airborne field observations of the wave field modulation by currents at the edge of an upwelling jet in Northern California and the Loop Current in the Gulf of Mexico. The results showed significant variability of the wave field, particularly for the wave breaking statistics, with the significant slope varying by ±15%, the directional spreading by ± 4°, and the whitecap coverage by ±50% or larger. The whitecap coverage correlated well with the spectral saturation and inversely with the directional spreading. Their measurements showed enhanced wave breaking along a submesoscale front at the edge of the upwelling jet and a reduction of the winds at 30 m above mean sea level, which is consistent with an increase of the drag along the front due to enhanced wave breaking. Raschke et al. (2014, 2016) developed techniques for the retrieval of surface current gradient information based on remote sensing measurements of ocean surface roughness, which were further validated with airborne remote observations against in situ measurements collected with surface drifters (Raschke et al., 2017). In this study, CEW is investigated numerically with the model WAVEWATCH III (WW3) forced by the Regional Ocean Modeling System (ROMS), and the Weather Research

* Corresponding author.

E-mail address: leromero@eri.ucsb.edu (L. Romero).

and Forecasting Model (WRF) with a realistic model configuration at very high resolutions O(100 m) in Southern California.

Wave models in Southern California have commonly focused on the swell band without external forcing by winds or currents (O'Reilly and Guza, 1993, 1998; O'Reilly et al., 2016; Crosby et al., 2016). The lack of wind forcing has resulted in significant errors in sheltered areas, particularly in the Santa Barbara Channel. The work by Rogers et al. (2007) with the model Simulating Waves Nearshore (SWAN) forced with global operational winds and wave boundary conditions from operational WAVEWATCH III (WW3) concluded that both boundary conditions and atmospheric forcing are critical for the model performance within the Bight. The recent study by Cao et al. (2018) with SWAN forced with WRF and boundary conditions from global reanalysis by European Centre Medium-Range Weather Forecasts (ERA-Interim) found qualitative agreement against buoy observations for a 10 year period. They also suggest that currents can significantly affect the wave field within the Bight.

This study expands on previous studies by investigating CEW, including wave breaking, at very high model resolutions with a realistic model configuration. The manuscript is organized as follows. In Section 2 we described the model physics and configuration. The results are presented in Section 3, followed by a discussion and conclusions in Sections 4 and 5, respectively.

2. Methods

The wave model WAVEWATCH III (The WAVEWATCH III Development Group [WW3DG], 2016) was implemented in Southern California. The spectral evolution of the directional wave spectrum $F(\mathbf{k})$ is modeled through the wave action conservation equation

$$\frac{\partial N(\mathbf{k})}{\partial t} + \frac{\partial}{\partial \mathbf{x}} \cdot \dot{\mathbf{x}} N(\mathbf{k}) + \frac{\partial}{\partial \theta} \dot{\theta} N(\mathbf{k}) + \frac{\partial}{\partial \mathbf{k}} \dot{\mathbf{k}} N(\mathbf{k}) = \frac{S_{in} + S_{nl} + S_{ds} + S_{bot}}{\sigma}, \quad (1)$$

$$\dot{\mathbf{x}} = (\mathbf{c}_g + \mathbf{u}), \quad (2)$$

$$\dot{\theta} = -\frac{1}{k} \frac{\partial \sigma}{\partial h} \frac{\partial h}{\partial m} - \mathbf{k} \cdot \frac{\partial \mathbf{u}}{\partial m}, \quad (3)$$

$$\dot{\mathbf{k}} = -\frac{\partial \sigma}{\partial h} \frac{\partial h}{\partial s} - \mathbf{k} \cdot \frac{\partial \mathbf{u}}{\partial s}, \quad (4)$$

where $N(\mathbf{k}) = F(\mathbf{k})/\sigma(k)$ is the wave action, with $F(\mathbf{k})$ being the directional wavenumber spectrum, $\sigma(k) = (gk \tanh kh)^{1/2}$ is the frequency according to the dispersion relationship, h is the water depth, $\mathbf{c}_g = \partial \sigma / \partial \mathbf{k}$ is the group velocity, and \mathbf{u} is the surface current vector, s is a coordinate in the θ direction, and m is a coordinate perpendicular to s (Tolman and Booij, 1998). The second term on the left side of Eq. (1) is the advection, the third term is the refraction, and the fourth term is direct forcing by topography and current variations, all three contributing to WEC through \mathbf{u} . The source terms on the right side of Eq. (1) correspond to the wind energy input S_{in} , nonlinear energy flux due to wave-wave resonant interactions S_{nl} , energy dissipation due to wave breaking S_{ds} , and energy loss due to bottom friction S_{bot} .

The directional wavenumber spectrum $F(\mathbf{k})$ is defined such that

$$E = \langle \eta^2 \rangle = \iint F(\mathbf{k}, \theta) k d\mathbf{k} d\theta, \quad (5)$$

where $\langle \eta^2 \rangle$ is the variance of the sea surface elevation. The corresponding azimuth integrated or omnidirectional spectrum is given by

$$\phi(k) = \int F(\mathbf{k}, \theta) k d\theta. \quad (6)$$

Note that within WW3 the factor of k on the right-hand side of Eqs. (5) and (6) is absorbed in the definition of the directional spectrum. WAVEWATCH III solves the wave action conservation equation (1) in the wavenumber domain and outputs preselected parameters over the entire configuration and the directional spectrum at selected points in terms of the relative frequency ($f = \sigma/(2\pi)$) according to

$$F(f, \theta) = \frac{2\pi k}{c_g} F(k, \theta), \quad (7)$$

with corresponding frequency spectrum

$$\Psi(f) = \int F(f, \theta) d\theta. \quad (8)$$

2.1. Model physics

The first three source terms on the right side of Eq. (1) are related to wind-wave generation. The wind input S_{in} is modeled according to Ardhuin et al. (2010) based on the quasilinear theory by Janssen (1989, 1991) including sheltering at short waves due to longer waves and swell dissipation. The nonlinear energy fluxes S_{nl} are computed with the Discrete Interaction Approximation (DIA — Hasselmann and Hasselmann, 1985), and the energy dissipation due to deep-water wave breaking S_{ds} is modeled according to Romero (2019) within the framework of Phillips' A distribution (Phillips, 1985), which was validated against the field measurements by Sutherland and Melville (2013). The wave breaking model S_{ds} is summarized below for completeness. The bottom friction is computed with a parameterization for a movable sandy bed by Ardhuin et al. (2003), switch option BT4 of WW3. The source terms were integrated allowing the resolved tail to evolve freely without a prognostic tail (Romero and Melville, 2010b; Liu et al., 2019).

2.2. Wave breaking model

The spectral dissipation $S_{ds}(\mathbf{k})$ is computed through $\Lambda(\mathbf{k})$, which is the length of breaking crest per unit bandwidth and unit area, according to

$$S_{ds}(\mathbf{k}) = -\frac{b(k)}{g^2} \Lambda(\mathbf{k}) c^5, \quad (9)$$

where $b(k)$ is the strength of breaking and is modeled with a threshold dependence on the omnidirectional saturation $B(k) = \phi(k)k^3$ as

$$b(k) = A(B(k)^{1/2} - B_T^{1/2})^{5/2}, \quad (10)$$

with $A = 3.8$ and $B_T = 1.1 \times 10^{-3}$ (Romero et al., 2012).

The $\Lambda(\mathbf{k})$ distribution is modeled as

$$\Lambda(\mathbf{k}) = \frac{l}{k} \exp\left(-\frac{B_{br}}{B(k)}\right) M_L(\mathbf{k}) M_W(k), \quad (11)$$

where the exponential factor dependent on the two-dimensional saturation $B(k) = F(k)k^4$ is based on a scaling of wave slope statistics assuming self similarity with $B_{br} = 5 \times 10^{-3}$ and $l = 3.5 \times 10^{-5}$. The function $M_L(\mathbf{k})$ accounts for the breaking modulation by the longer waves, and $M_W(k)$ is a breaking amplification for the short waves to balance the wind input.

The wave breaking modulation due to longer waves is modeled according to

$$M_L(\mathbf{k}) = \left(1 + 400 \sqrt{\text{cmss}(k)} \cos^2(\theta - \theta_w)\right)^{3/2}, \quad (12)$$

where the cumulative mean-squared slope

$$\text{cmss}(k) = \int_0^k \phi(k) k^2 dk, \quad (13)$$

and θ_w is the spectrally weighted mean wave direction defined as

$$\theta_w = \text{atan}\left(\frac{\int F(\mathbf{k}) \sin \theta d\mathbf{k}}{\int F(\mathbf{k}) \cos \theta d\mathbf{k}}\right). \quad (14)$$

The anisotropic function $M_L(\mathbf{k})$ controls the directional spreading and it was tuned against the measurements by Romero and Melville (2010a). The wind modulation function is modeled linearly according to

$$M_W(k) = \frac{1}{1.9} (1 + 0.9 \max[1, \frac{k}{k_o}]) \quad (15)$$

with $k_o(u_*) = g(\frac{3}{28d_*})^2$. Thus, $M_W(k)$ is greater than one for $k/k_o > 1$ and equal to one otherwise, balancing the wind input at large

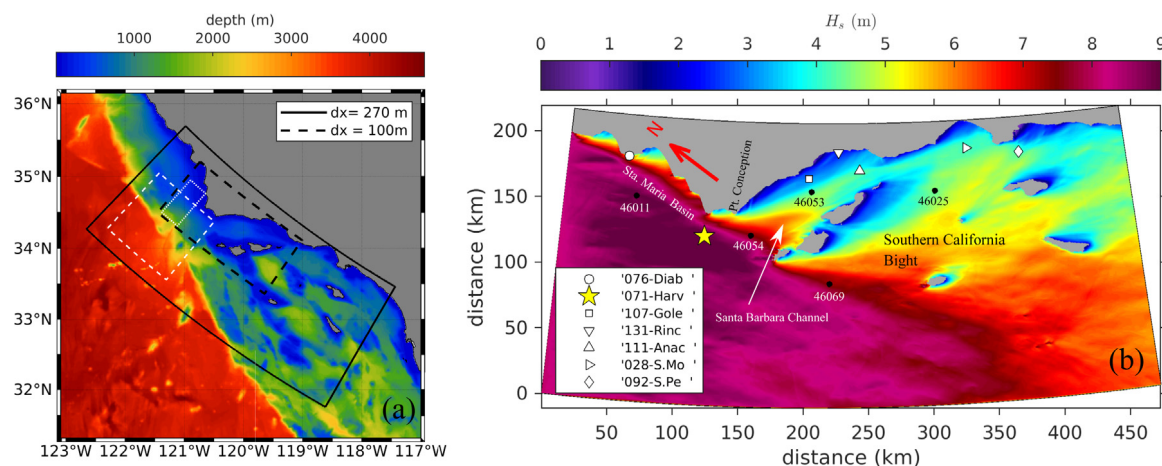


Fig. 1. (a) Nested model configurations in Southern California with horizontal resolutions of 270 m (L2) and 100 m (L3) shown with black solid and dashed lines, respectively. (b) Snapshot of computed L2 significant wave height H_s on Dec 28 at 3:00 am (UTC). The domain is rotated along the longest axis. Boundary conditions were generated using the buoy observations at Harvest buoy (yellow star). Model output is validated against observations from all other buoys shown in the legend from CDIP and the National Data Buoy Center (NDBC) shown with black circles. Gray areas correspond to land and islands. Dotted and dashed white boxes in (a) show areas used to compute statistics outside the Southern California Bight.

wavenumbers to maintaining a saturation level approximately consistent with the field observations (i.e., Romero and Melville, 2010a and Lenain and Melville, 2017).

By definition, the total length of breaking crests per unit surface area L is given by

$$L = \int \Lambda(k) dk \quad (16)$$

and higher moments of $\Lambda(k)$ are related to different physical parameters. Assuming that the phase speed of waves is proportional to the speed of the breaking fronts,¹ the probability of breaking at a point corresponds to $p_b = \int \Lambda(k) c dk$. Following Kleiss and Melville (2010), the whitecap coverage is modeled according to

$$W = \frac{2\pi}{g} \gamma \int c^2 \Lambda(k) dk, \quad (17)$$

where γ is a dimensionless factor representing the duration of breaking relative to the wave period ($2\pi c/g$). The factor of γ here is 30% larger than that of Romero (2019) to account for the limited bandwidth.

The rate of air volume entrained by breaking waves per unit area V_A is modeled according to Deike et al. (2017) as given by

$$V_a = \frac{\chi A}{g} \int (B^{1/2}(k) - B_T^{1/2})^{3/2} c^3 \Lambda(k) dk, \quad (18)$$

where A is the proportionality factor of the strength of breaking (10), and $\chi = 0.2$ is a constant representing the ratio between the work done by buoyancy forces and mechanical dissipation.

2.3. Model configuration

WW3 was implemented using a ROMS nested configuration described in Dauhajre et al. (2019), specifically the 270 m (L2) and 100 m (L3) configurations which are shown in Fig. 1a. The largest L0 domain with a resolution of 4 km covers the entire U.S. West Coast as described by Renault et al. (2016). The model is hydrostatic and does not assimilate observations, instead the L0 boundary conditions are from the Simple Ocean Data Assimilation (SODA) reanalysis (Carton and Giese, 2008). Barotropic tides are introduced at the boundaries of the next level of nesting L1 with a resolution of 1 km. The L2 and L3 bathymetry consists of the SRTM30-PLUS dataset (Becker et al., 2009) blended with the NOAA-NGDC coastal relief dataset. The wind forcing is from a regional implementation of the Weather and Research

Forecasting model (WRF) with a horizontal resolution of 6 km (Renault et al., 2016). The ROMS configuration without data assimilation is expected to produce realistic mesoscale and submesoscale features in a statistical sense as opposed to deterministic (e.g., Buijsman et al., 2012; Romero et al., 2013; Uchiyama et al., 2014; Romero et al., 2016). The solutions also include hydrostatic internal tides which are only evident in certain regions as they become incoherent from their interaction with mesoscale and submesoscale processes (Van Haren, 2004; Ponte and Klein, 2015; Kumar et al., 2019).

Two periods were selected for this study: the month of December 2006 and the period between March 15 through April 15 in 2007. The periods were chosen because of the relatively active wave climate with the significant wave height (H_s) reaching 8.5 m in the winter and 5.5 m in the spring in exposed areas. Wave boundary conditions were generated using buoy observations at the Harvest buoy from the Coastal Data Information Program (CDIP). Other buoys with supporting wind and wave observations within the domain were used for model validation. A total of 7 CDIP buoys collected wave measurements during the periods of interest which are in order from the North: Diablo Canyon, Harvest, Goleta, Rincon, Anacapa, Santa Monica, and San Pedro Canyon (see locations in Fig. 1b). Five buoys from the National Data Buoy Center (NDBC) collected wind and wave observations (46011, 46054, 46053, 46025, 46069 — see Fig. 1b), with the exception of 46011 which did not operate during the Winter. The deep-water buoys exposed to open ocean swell are the Harvest buoy, 46011 in the Santa Maria Basin, and 46069 south of Santa Rosa Island. Following O'Reilly et al. (2016), the Harvest buoy data was used to generate boundary conditions accounting for the appropriate time lag determined by the distance between a given boundary point and the buoy divided by the deep-water group speed. This was done at all frequencies and directions projected along the shortest path to the buoy location. Prior to calculating the boundary conditions, the buoy observations (i.e. frequency spectra and directional Fourier coefficients) at half-hour intervals were temporally smoothed using a running filter (11 point Hann window) with an effective decorrelation timescale of 2.5 h. There are many ways to calculate the directional distribution from buoy measurements, all of which are method dependent (Benoit, 1992). The two most widely used methods to estimate wave directional distribution are the Maximum Likelihood Method (Capon, 1969) and the Maximum Entropy Method (Lygre and Krogstad, 1986). We used the Maximum Entropy Method which gives narrower spectra and is the preferred method used by CDIP due to the narrowness of the swell band. Since the predominant waves during spring and winter in Southern California are from the

¹ See discussion in Romero (2019).

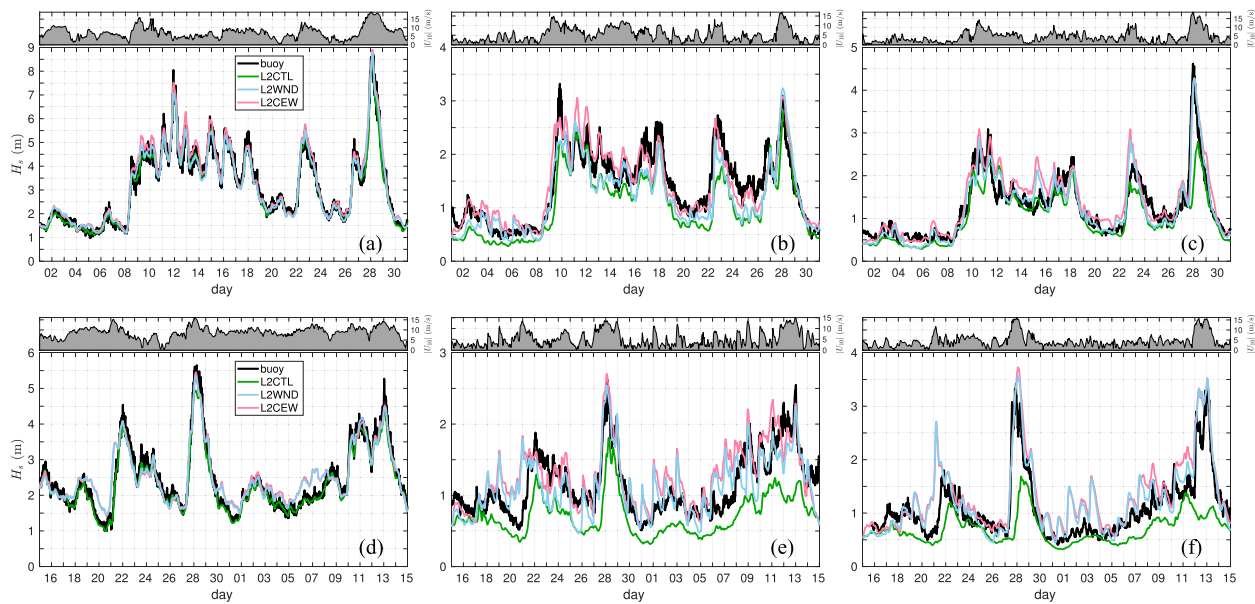


Fig. 2. Significant wave height (H_s) for the one-month long solutions from December 1st 2006 to January 1st 2007 (a–c) and March 15 to April 15 2007 (d–f) at Harvest (a, d), Goleta (b, e), and San Pedro (c, f) buoys. The buoy measurements are shown in black, and ww3 solutions in green, light blue, and pink, corresponding to the control (CTL) without forcing, forced by winds (WND), and forced by winds and currents (CEW), respectively. The wind speed time series interpolated at the buoy locations from WRF are shown on top of each panel.

Table 1

Model runs and their name. The control (CTL) runs do not include any external forcing. All other runs include bottom friction and depth-induced dissipation. Wind forced solutions (WND) include wind forcing, resonant energy fluxes, and deep-water wave breaking. Runs accounting for current effects on waves (CEW) are forced by both winds and currents.

Label	Res. (m)		Wind	CEW
	270	100		
L2CTL	X			
L2WND	X		X	
L2CEW	X		X	X
L3CTL		X		
L3WND		X	X	
L3CEW		X	X	X

NW/W, boundary conditions generated only using the Harvest buoy are sufficient. For other seasons with significant wave energy coming from the South other buoys can be combined to provide adequate boundary conditions (e.g., O'Reilly et al., 2016).

The spectral grid used consists of 24 directions ($\Delta\theta = 15^\circ$), and 22 frequencies between 0.037 and 0.7 Hz with logarithmic increment $\Delta f/f = 0.15$. The choice to use a relatively coarse grid as opposed to the standard grid with $\Delta f/f = 0.1$ was to reduce the computational cost. Preliminary tests showed that our results were not sensitive to using a coarser grid. The propagation scheme used is the third-order ULTIMATE QUICKEST with spatial averaging (Tolman, 2002). Several runs were carried out for comparison, including control runs with depth-induced refraction only without external forcing (CTL), runs forced by wind (WND), and runs forced by both wind and currents (CEW). Surface currents from ROMS were used to force the model using the vertical grid point closest to the surface. This choice was made for simplicity but it would be more appropriate to use scale and depth dependent current velocities (Stewart and Joy, 1974) at the expense of increasing the number of input parameters into WW3. The model runs are summarized and labeled in Table 1. The L2 (L3) global and source term time steps were set to 40 s (12 s), with spatial and intra-spectral propagation time steps of 8 s (4 s) and 20 s (6 s), respectively. Model output was saved at hourly intervals which is composed of directional wave spectra at the buoy locations and gridded output. The gridded output includes

- significant wave height $H_s = 4 E^{1/2}$
- mean wave period or so-called energy period $T_{0,-1} = E^{-1} \int \Psi(f) f^{-1} df$
- mean wave direction $\theta_w = \text{atan} \left(\frac{b}{a} \right)$, with $a = \int \int F(f, \theta) \cos \theta df d\theta$ and $b = \int \int F(f, \theta) \sin \theta df d\theta$
- directional spreading $\sigma_\theta = \left[2 \left\{ 1 - \left(\frac{a^2 + b^2}{E^2} \right)^{1/2} \right\} \right]$ (Kuik et al., 1988)
- mean square slope $mss = \int \Psi(f) |k|^2 df$
- surface Stokes Drift $u_{s0} = g \int \int \frac{\cosh 2kh}{\sinh^2 kh} k F(f, \theta) df d\theta$
- friction velocity u_*
- whitecap coverage W
- air-entrainment rate V_A
- total energy dissipation due to breaking $E_{ds} = \rho g \int \int S_{ds}(f, \theta) df d\theta$

Note that the resolved mss only accounts for a small fraction of the total mss without the contribution from short gravity and gravity-capillary waves (Cox and Munk, 1954).

3. Results

3.1. Model performance

The performance of WW3 is evaluated against the buoy observations. Time series of the significant wave height H_s for the L2 configurations at Harvest, Goleta, and San Pedro Canyon are compared against the buoy data in Fig. 2. The comparison at Harvest buoy is in excellent agreement serving as a check for the boundary conditions. The model solutions within the Southern California Bight at Goleta and San Pedro buoys without wind forcing significantly underestimate H_s with larger errors in the Spring. The solutions forced by wind (WND) show significant improvement with good agreement with the observations particularly during large wave events but with appreciable errors at higher temporal variability (~ diurnal). The high-frequency variability of the H_s solutions forced by wind shows good correspondence with the local wind variability from WRF (shown on the top of each panel). The model solution forced by both winds and currents (CEW) generally tracks the solution only forced by wind (WND). However, occasionally the CEW solution shows significant deviations at the Goleta buoy within

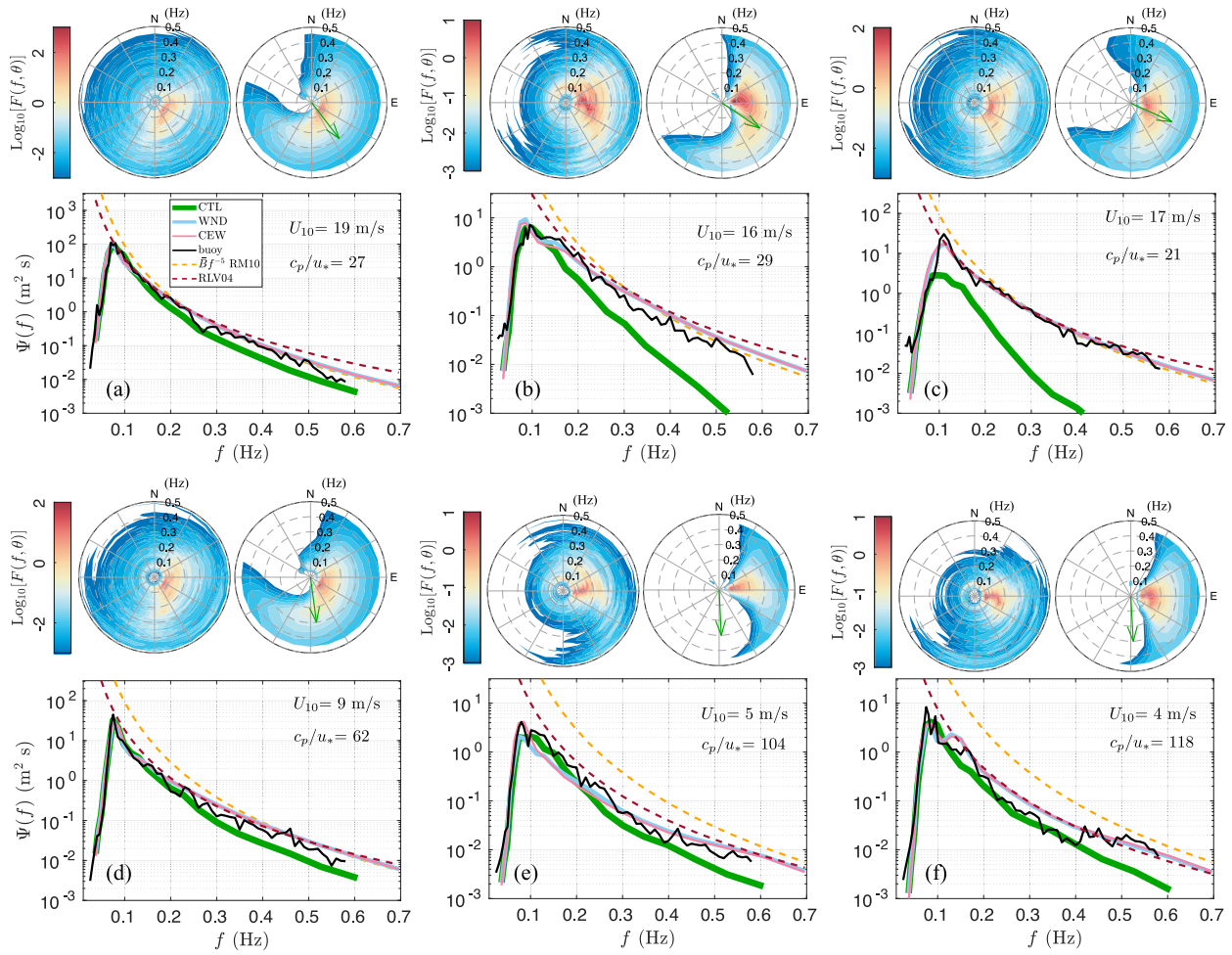


Fig. 3. Wave spectra at (a, d) Harvest, (b, e) Goleta and (c, f) San Pedro Canyon during the largest storm on Dec. 28, 2006 00:00 (UTC) and a swell dominated period on Dec. 18, 2006 06:00 (UTC) shown in the top and bottom panels, respectively. The 1d frequency spectra compare buoy measurements against model solutions from the control (CTL — green), wind forced (WND — blue) and CEW (pink) experiments. The orange and maroon dashed lines show the saturation level by Romero and Melville (2010a), and the f^{-4} equilibrium range spectrum by Resio et al. (2004). The directional spectra on top of each panel shows the buoy data (left) and wind forced solution (right). The green arrows indicate the WRF wind direction. The wind speed and wave age c_p/u_* are indicated in each panel, where c_p is peak phase speed, and u_* is the friction velocity.

the Santa Barbara Channel during periods of relatively low winds (< 10 m/s), see for example 12/13 and 12/17 in Fig. 2b, and 3/24 and 3/27 in Fig. 2e).

Direct comparisons of omnidirectional and directional frequency spectra during the largest storm on Dec. 28 00:00 (UTC) and a period of low wind dominated by swell on 12/18 6:00 (UTC) at Harvest, Goleta, and San Pedro buoys are shown in Figs. 3a–c and 3d–f, respectively. As expected, the control run underestimates the energy, particularly at high frequencies with smaller errors during low winds. The wind forced spectra are in good agreement with the buoy observations at all three buoys. During the storm, the observations and model approximately match the saturation spectrum ($\frac{g^2}{2\pi^2} \bar{B} f^{-5}$) by Romero and Melville (2010a) at frequencies larger than 0.2 Hz. At lower wavenumbers and lower wind speeds the spectral tail is better represented by the f^{-4} equilibrium range model by Resio et al. (2004). The corresponding directional spectra forced by wind (WND) compare qualitatively well against the buoy measurements for the two periods shown. However, as shown in Fig. 2 the model errors can be significant at times, partly due to wind forcing errors as can be seen in the high-frequency fluctuation in Fig. 2e, f correlated to wind fluctuations. The CEW solutions are also shown generally tracking the WND solutions with larger differences near the spectral peak at the Goleta buoy in low winds (Fig. 3e).

The overall model performance is further quantified at each buoy for the two periods in Table 2. Given a variable X the normalized

root-mean-square error is defined as

$$\text{NRMSE}(X) = \sqrt{\frac{\sum (X_{\text{mod}} - X_{\text{obs}})^2}{\sum X_{\text{obs}}^2}}, \quad (19)$$

and the normalized bias

$$\text{NB}(X) = \frac{\sum (X_{\text{mod}} - X_{\text{obs}})}{\sum X_{\text{obs}}}, \quad (20)$$

where X_{obs} and X_{mod} correspond to the observations and model data, respectively (Ardhuin et al., 2010).

The normalized bias of H_s for the control experiment is generally negative and significant within the Southern California Bight, particularly during the spring, reaching values as low as -38% at the Goleta buoy in the Santa Barbara Channel. These biases are improved with the wind forced solution except at the Santa Monica buoy. In contrast, the NRMSE's between the control and the solution forced by wind are not very different. The solutions forced by winds and currents give generally larger errors than the wind forced solution except for NB at the Goleta buoy for the winter solution. The overall average NB and NMRSE for both seasons give -11% and 23% for the control, 5% and 21% for the wind forced solution, and 11% and 22% for the CEW solution, respectively. The overall positive bias for the wind forced runs is consistent with the positive bias of the wind speed shown in Table 2. Also, the NRMSE of the wind speed is significant, on average 54% , which also contributes to the wave model performance. Both

Table 2

Normalized bias and Normalized root-mean-square error (NRMSE) for the significant wave height in the L2 (270 m) configuration and forcing wind speed against the buoy data for the two periods considered, Winter 2006 and Spring 2007. Buoys are listed in order from the N.

Buoy	U_{10}		H_s						U_{10}		H_s					
	NB %	NRMSE %	NB %			NRMSE %			NB %	NRMSE %	NB %			NRMSE %		
			CTL	WND	CEW	CTL	WND	CEW			CTL	WND	CEW	CTL	WND	CEW
Winter 2006																Spring 2007
076-Diablo C.			+6	+6	+8	15	17	19			-3	0	-2	10	12	12
46011									+16	42	+2	+7	+7	10	14	14
071-Harvest			-3	-1	+4	5	6	8			-5	+3	+4	7	12	12
46054	-6	53	+4	+6	+6	11	14	15	+2	35	-2	+9	+7	10	17	16
107-Goleta			-25	-14	+1	28	23	18			-38	-2	11	40	25	26
131-Rincon			-13	-3	+3	24	22	22			-26	+13	20	34	30	34
46053	+37	64	-13	-6	+1	17	16	12	+38	66	-22	+7	+12	26	25	26
111-Anacapa			-8	+2	+4	20	19	20			-23	+8	11	32	26	28
46025	+16	57	-12	+5	+16	21	18	23	+24	56	-26	+20	+28	37	33	38
028-S. Monica			+11	+23	+30	27	32	38			+14	+25	+24	31	34	34
092-S. Pedro			-16	-3	+11	28	19	23			-35	+14	+22	48	31	34
46069	+2	46	+5	+9	+7	13	14	13	+12	36	-5	+12	+10	14	20	20
Average	+12	55	-5	2	8	19	18	19	+18	47	-14	10	13	25	23	25

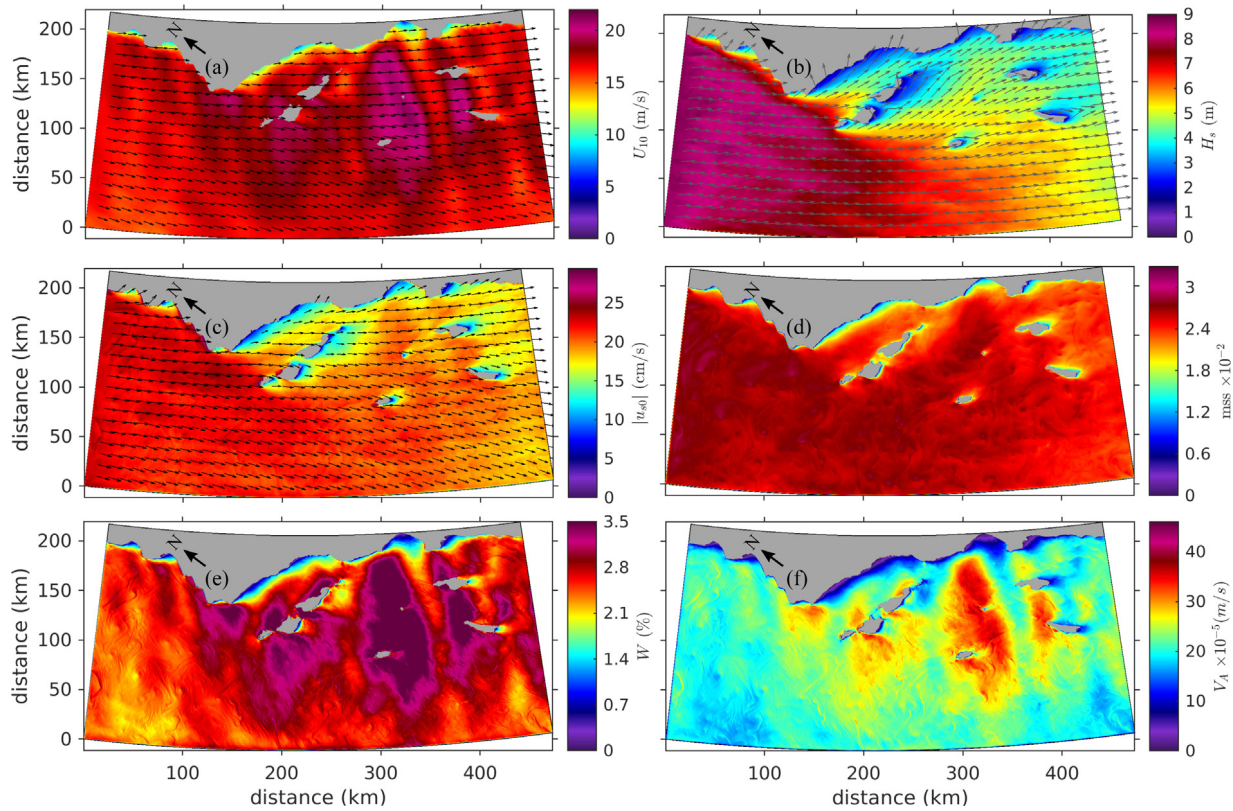


Fig. 4. (a) Surface wind speed U_{10} and direction, (b) significant wave height H_s and mean wave direction, (c) surface Stokes drift u_s , (d) mean square slope mss, (e) whitecap coverage W , and (f) air-entrainment rate V_A on 12/28/2006 00:00 (UTC) during a strong winter storm. Vectors (a–c) were subsampled by a factor of 40 corresponding to approximately 10 km spacing. Wave solutions include forcing from wind and currents (L2CEW).

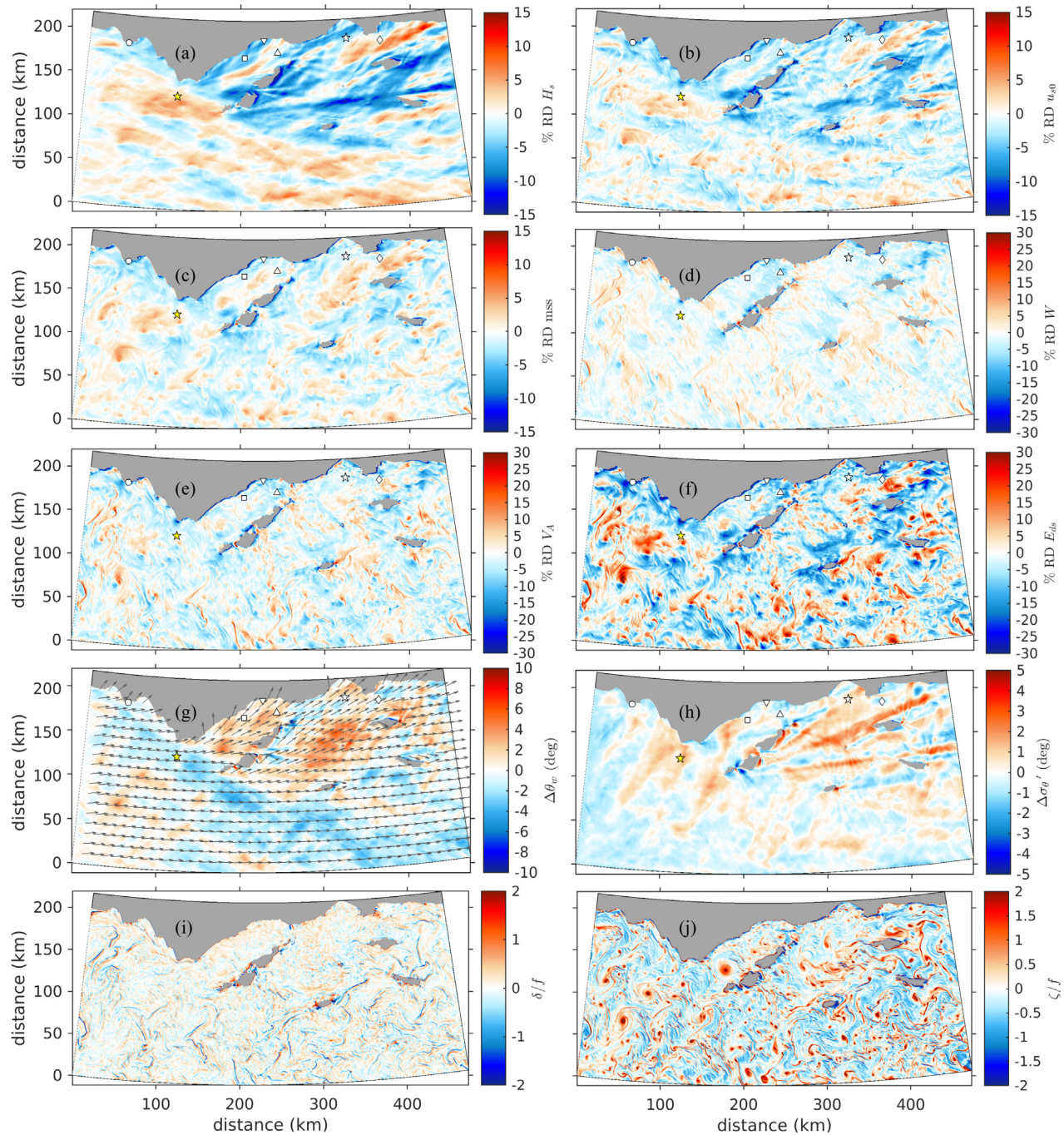


Fig. 5. Model differences between solutions forced by winds and currents (L2CEW) and wind-only (L2WND) comprised of the relative difference RD (%) for (a) H_s , (b) u_{s0} , (c) mss, (d) W , (e) V_A , and (f) E_{ds} , (g) mean wave direction difference $\Delta\theta_w$, and (h) directional spreading difference anomaly $\Delta\sigma_\theta'$ (without the spatial mean). The surface current divergence and vorticity normalized by the Coriolis frequency are shown in (i) and (j), respectively. The data shown is from 12/28/2006 00:00 (UTC) during a strong winter storm corresponding to Fig. 4. The arrows in (g) indicate the mean wave direction L2WND subsampled at 10 km spacings.

wind and currents can enhance H_s within the Bight, especially the wind. The winds can significantly improve the model performance in sheltered areas, particularly during strong wind events. However, NRMSE values are not much improved with wind or wind and currents, which is probably a combination of the need for better physics but more important phase discrepancies because of WRF and ROMS are not assimilative and thus are event/location inaccurate. Regarding the physics, other nonlinear processes not accounted for may be important, such as diffraction, coherent interference, and triad resonant interactions. Other errors may come from inaccuracies of the approximate four-wave resonant interactions and the parameterizations of wind forcing, wave breaking, and bottom dissipation.

3.2. Examples and differences due to CEW

In this section, CEW is analyzed by comparing the solutions forced by winds (WND) to those forced by both winds and currents (CEW) under different wind forcing conditions and different model resolutions (L2 and L3). Fig. 4 shows L2 snapshots during the strongest winter storm on 12/28 composed of wind speed and direction, H_s and mean wave direction, surface Stokes drift (u_{s0}), mean square slope mss, whitecap coverage W , and air-entrainment rate due to breaking V_A . The wind is on average from the northwest reaching speeds of up to 20 m/s. The incoming waves are also from the northwest with H_s reaching 8 m outside the Bight. The surface Stokes drift, mss, W , and V_A show

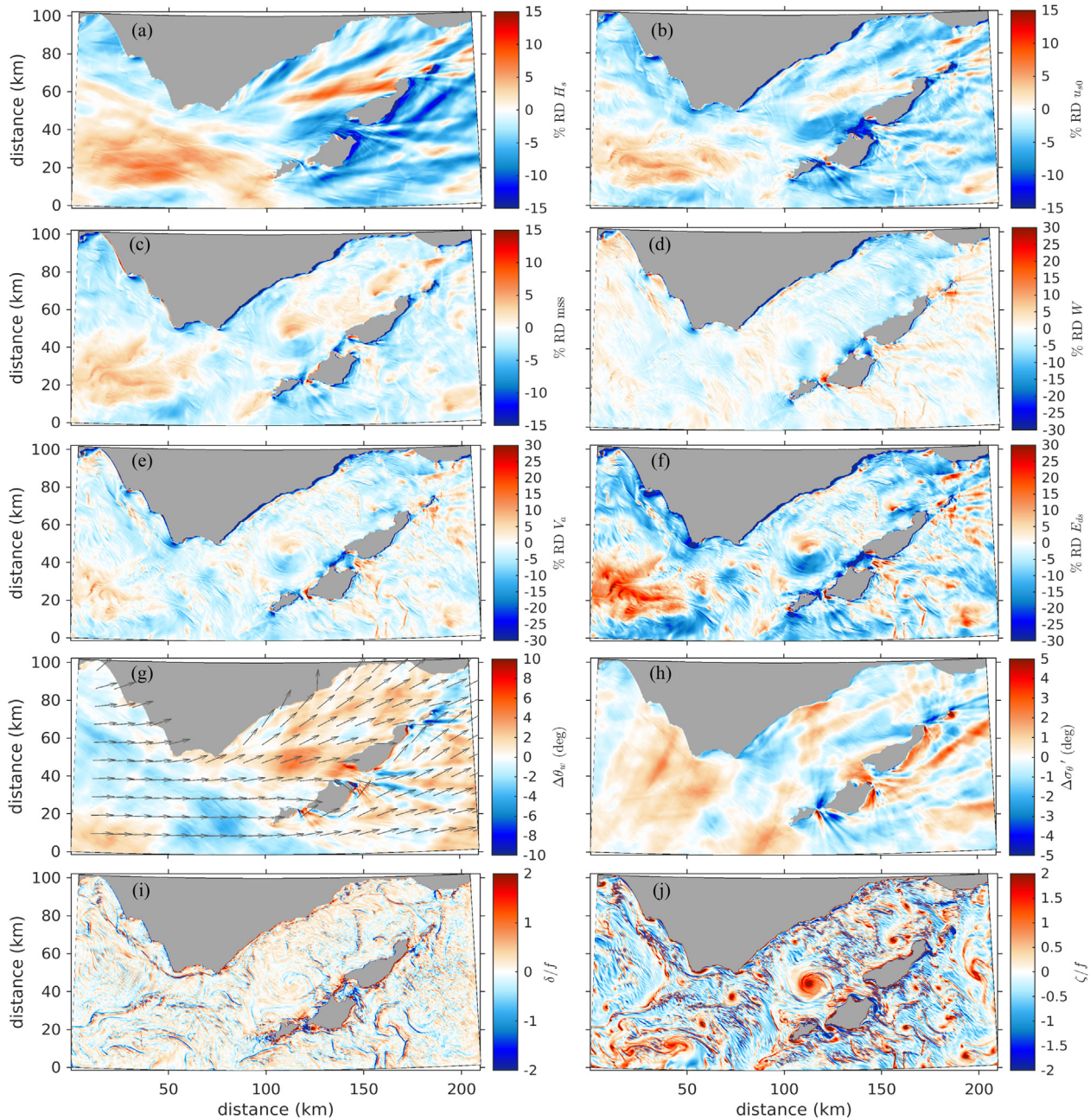


Fig. 6. Same as in Fig. 5 for the L3 configuration.

good correspondence with the wind field with additional small scale variability due to currents. To further characterize CEW, the output is analyzed through relative differences between the solution forced by wind and currents (CEW) and that only forced by wind (WND). For a given variable X the relative difference in percent corresponds to

$$\text{RD}(X) = (X^{\text{CEW}} / X^{\text{WND}} - 1) \times 100\%, \quad (21)$$

where the subscripts WND and CEW indicate the corresponding solution. We also consider the angle differences in mean wave direction $\Delta\theta_w = \theta_w^{\text{CEW}} - \theta_w^{\text{WND}}$ and directional spreading difference $\Delta\sigma_\theta = \sigma_\theta^{\text{CEW}} - \sigma_\theta^{\text{WND}}$.

The model differences for the timeframe in Fig. 4 with strong winds are shown in Figs. 5 and 6, corresponding to the L2 and L3 configurations, respectively. Panels a-f show relative differences RD of H_s , u_{s0} , mss, W , V_a , and E_{ds} , respectively. The mean wave direction difference $\Delta\theta_w$ and directional spreading difference anomaly $\Delta\sigma_\theta'$, without the spatial mean, are shown in panels g and h, respectively. The surface current divergence $\delta = u_x + v_y$ and relative vorticity $\zeta = v_x - u_y$

normalized by the Coriolis frequency f are shown in Figs. 5i,j and Figs. 6i,j. The H_s RD values are within $\pm 5\%$ in open ocean, reaching $\pm 15\%$ in sheltered regions, which is consistent with what we see comparing to buoy observations. The RD values of the surface Stokes drift and mss show similar patterns to that for H_s but with increased small scale variability that correlates with the surface current relative vorticity and divergence (Figs. 5i,j and 6i,j). The breaking variables give larger RD magnitudes reaching 15%, 20%, and 30% for W , V_a , and E_{ds} , respectively, and their distributions show good correspondence to the vorticity and divergence fields. The spatial distributions for the difference in mean wave direction $\Delta\theta_w$ in open ocean, away from sheltered regions, show good correspondence with relative differences of H_s , and those for u_{s0} to a lesser extent. Similarly, the directional spreading difference anomalies $\Delta\sigma_\theta'$ show inverse relationships with the whitecap coverage W , being qualitatively consistent with the observations by Romero et al. (2017) with increased breaking where the spectrum is narrower. The directional spreading biases due to CEW calculated as

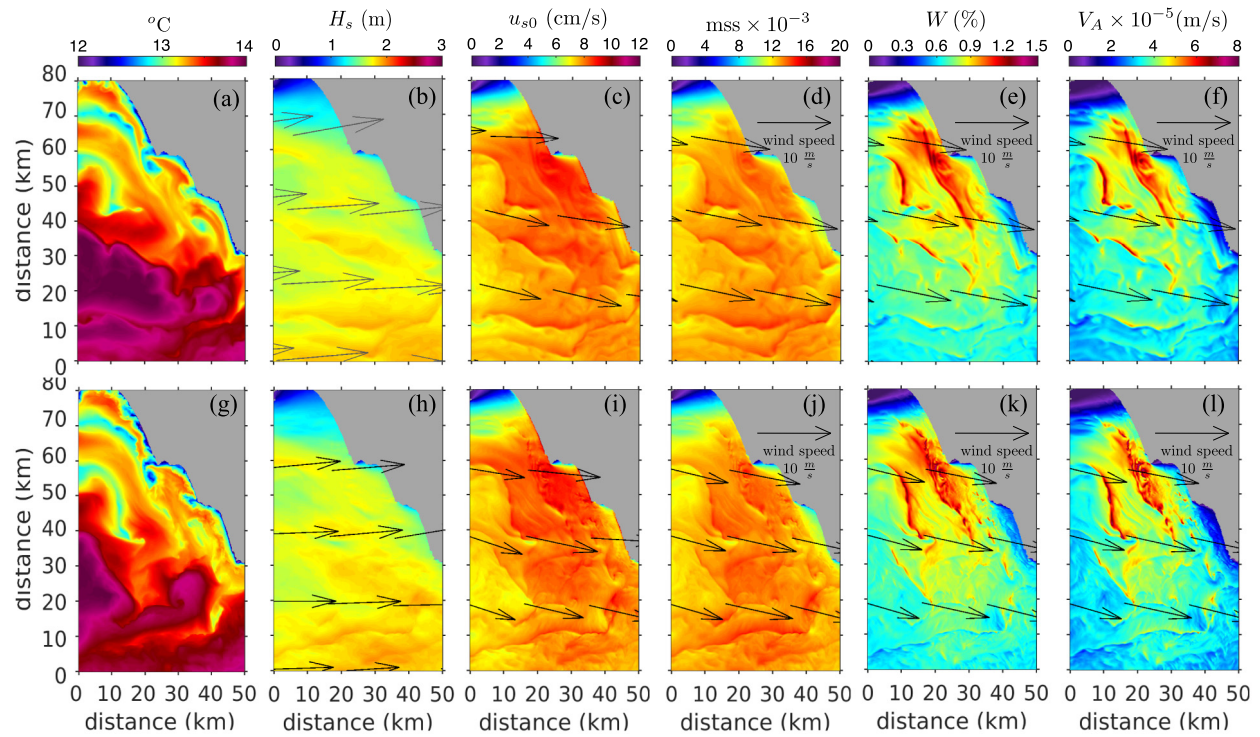


Fig. 7. Snapshots of L2 (a–f) and L3 (g–l) model solutions zooming over the Santa Maria Basin north of Point Conception on 12/30/2006 00:00 (UTC) under light wind forcing ($\sim 10 \text{ m/s}$) after the passage of the strong winter storm shown in Fig. 4. (a, g) Sea surface temperature, (b, h) Significant wave height H_s and peak wave direction, (c, i) surface Stokes drift u_{s0} , (d, j) mean square slope mss, (e, k) whitecap coverage W , and (f, l) air-entrainment rate V_A . Vectors were subsampled at 20 km spacings. Wave solutions were forced by both wind and currents (L2CEW and L3CEW).

the spatial average of $\Delta\sigma_\theta$ for the data shown is 0.7° and 0.85° for L2 and L3, respectively.

Model snapshots of H_s , u_{s0} , mss, W , and V_A zooming over the Santa Maria Basin outside the Southern California Bight during relatively low winds ($\sim 10 \text{ m/s}$) for the L2 and L3 configurations are shown in Fig. 7. We focus on the Santa Maria Basin in open ocean unaffected by the shadowing and sheltering from land and islands within the Bight. Just as was shown with the high wind event, the data exhibit fine-scale structure which increases relatively from H_s followed by u_{s0} , mss, W , and V_A . The higher moments of the spectrum and breaking variables show strong modulation by cold filaments that can be observed on the north. There is also apparent modulation due to a cold-core eddy shed by the headland adjacent to it. The model differences for the low wind case are shown in Figs. 8a-h, and Figs. 9a-h corresponding to L2 and L3 solutions respectively, with corresponding normalized surface vorticity and divergence in panels (i) and (j). The mean wave direction differences $\Delta\theta_u$ show some correspondence with RD H_s , u_{s0} , and mss fields over particular regions, but the relationship is not very clear. Similarly the difference in directional spreading is not strongly linked to other RD variables, but in certain areas where the spectrum narrows breaking increases as seen earlier with the high wind case. The directional spreading bias due to CEW for this case is 1.9° and 2.2° , for L2 and L3, respectively. The relative differences, in particular the wave-breaking variables, show good correspondence with the current gradients (8i,j and 9i,j). The L2 RD magnitudes are much larger for the low wind example compared to the high wind case shown in Fig. 5. At lower winds the RD values reach magnitudes of about 12% for H_s , u_{s0} and mss, and 50%, 75% and 100% for W , V_A , and E_{ds} , respectively. The relative differences increase in magnitude with increasing resolution giving values for the L3 configuration reaching 15% in magnitude for H_s , and magnitudes of up to 70%, 100% and 120%, for W , V_A , and E_{ds} , respectively. It is expected that further increasing the resolution would increase the relative differences even more, specially for the higher moments and wave-breaking variables.

3.3. Statistical variability

The differences due to CEW are further explored with respect to the wind speed and model resolution over a 7 day period (12/26/2006–1/1/2007), which includes the largest winter storm. The statistical analysis was carried out over an area that overlaps with the L2 and L3 configurations, located north of Point Conception (dotted white box in Fig. 1). The root-mean-square (rms) relative differences (RD_{rms}) between solutions forced by winds and currents (CEW) and wind-only (WND) are plotted in Fig. 10a for the L2 and L3 solutions and the various wave parameters considered showing decreasing trends with increasing wind speed. The rms differences are largest for the total energy dissipation, followed by the air-entrainment and whitecap coverage, varying between 22% and 7%, 17% and 3%, and 14% and 2%, respectively. The rms differences for H_s , u_{s0} , and mss show a weaker decreasing trend with wind speed varying only between 5% and 2%. The impact of model resolution on the rms differences for the wave-breaking variables is relatively small and negligible at high winds. In contrast, the model resolution is negligible for the non-breaking variables across wind forcing regimes. The rms vorticity and divergence also decrease with increasing wind speed being significantly larger for L3 compared to L2 (Fig. 10d). The decrease of CEW with increasing wind speed is consistent with the decrease of rms vorticity and divergence. But also, as the wind increases the wind input and breaking restore the wave field to back to equilibrium much faster reducing CEW (Phillips, 1984).

The average probability density functions (pdf) of the relative difference normalized by the rms (RD/RD_{rms}) are plotted in Fig. 10b,c for the L2 and L3 configurations, respectively. The distributions across model resolutions are similar except that the tails of L3 distributions are longer. The RD pdf of H_s is approximately Gaussian (black dotted line) with approximately zero excess kurtosis, whereas that for u_{s0} and mss is on average 0.2. The wave breaking distributions have an average skewness and kurtosis of 1 and 4.6, respectively. The pdfs

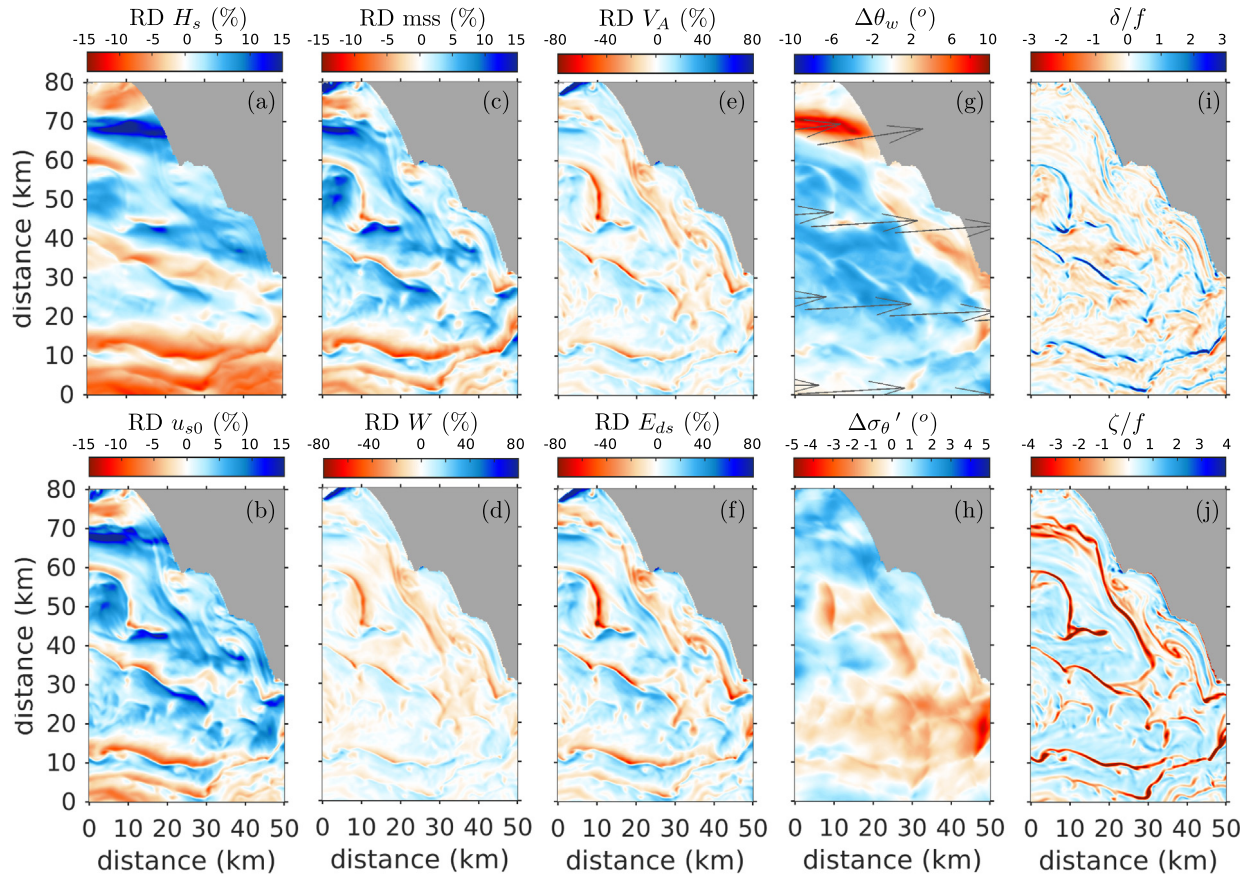


Fig. 8. Model differences between solutions forced by winds and currents (L2CEW) and wind-only (L2WND) zooming over an area outside of the Santa Barbara Channel north of Point Conception, within the Santa Maria Basin, comprised of the relative difference RD (%) for (a) H_s , (b) u_{s0} , (c) mss, (d) W , (e) V_A , and (f) E_{ds} , (g) mean wave direction difference $\Delta\theta_w$, and (h) directional spreading difference anomoly $\Delta\sigma_{\theta}'$ (without the spatial mean). The surface current divergence and vorticity normalized by the Coriolis frequency are shown in (i) and (j), respectively. The data shown is from 12/30/2006 00:00 (UTC) after the strong winter storm in Fig. 7. The arrows in (g) indicate the mean wave direction L2WND subsampled at 20 km spacings.

of the non-breaking variables are approximately symmetric, whereas the breaking distributions are positively skewed with longer tails. The positive skewness is consistent with the results by Phillips (1984) on the response of the spectral saturation due to convergent and divergent currents under the influence of wind forcing and dissipation due to breaking. His results showed the saturation response is asymmetric with a larger and highly localized enhancement due to convergence compared to the relative reduction at divergences. Not only is the response due to surface current convergence/divergence asymmetric, the statistics of surface current gradients at submesoscales are also skewed (McWilliams, 2016). In this analysis, the skewness is -1.1 and -1.4 for δ , and 2.1 and 2.4 for ζ of the L2 and L3 configurations, respectively.

3.4. Spatial variability

In this subsection, the spatial variability due to CEW is further assessed with wavenumber spectra of the relative differences. Spectra were calculated for the L3 configuration along the main axis of the white dotted box in Fig. 1a during the fourth week in December 2006 including the largest storm. Following Romero and Melville (2010a), prior to calculating a wavenumber spectrum data were interpolated on a regular grid at the model resolution, detrended, and tapered with a Hann window. The average spectra computed from the relative differences are shown in Fig. 11a and compared to the spectrum of the surface currents speed (u) scaled by a factor of 0.01 for clarity. The levels of the RD spectra are consistent with the rms values shown

in Fig. 10a with larger variability for the wave-breaking variables followed by mss and u_{s0} , and with the lowest variance for H_s . Similarly, the decrease of the spectra with increasing wavenumber is slowest for the wave-breaking variables followed by mss and u_{s0} with the RD H_s spectrum decreasing faster with \tilde{k} than the u spectrum. Here \tilde{k} denotes the wavenumber of the spectra for the wave variables to differentiate from that of the wave spectrum.

To better show the differences between spectra of the relative differences $PSD_{RD}(\tilde{k})$, we plot them in Fig. 11b normalized by the linear average of the spectral density for wavelengths greater than 10 km according to

$$\langle PSD_x \rangle = \frac{\int_{\tilde{k}_{min}}^{0.1 \text{ km}^{-1}} PSD_x(\tilde{k}) d\tilde{k}}{0.1 \text{ km}^{-1} - \tilde{k}_{min}}, \quad (22)$$

where $\tilde{k}_{min} = 1/66 \text{ km}^{-1}$ is the lowest number resolved in the analysis. The normalized H_s RD spectrum approximately traces the spectrum of the currents (u) but decays faster for scales shorter than 1 km. In contrast, the normalized spectra for u_{s0} , mss, and the wave-breaking variables deviate from the normalized u spectrum with increasing wavenumber showing larger differences for scales of order 1 km or smaller. The study by Arduhin et al. (2017) at scales between 5 km and 200 km similarly reported larger variability at shorter scales for the higher moments which are dominated by shorter wave components compared to H_s .

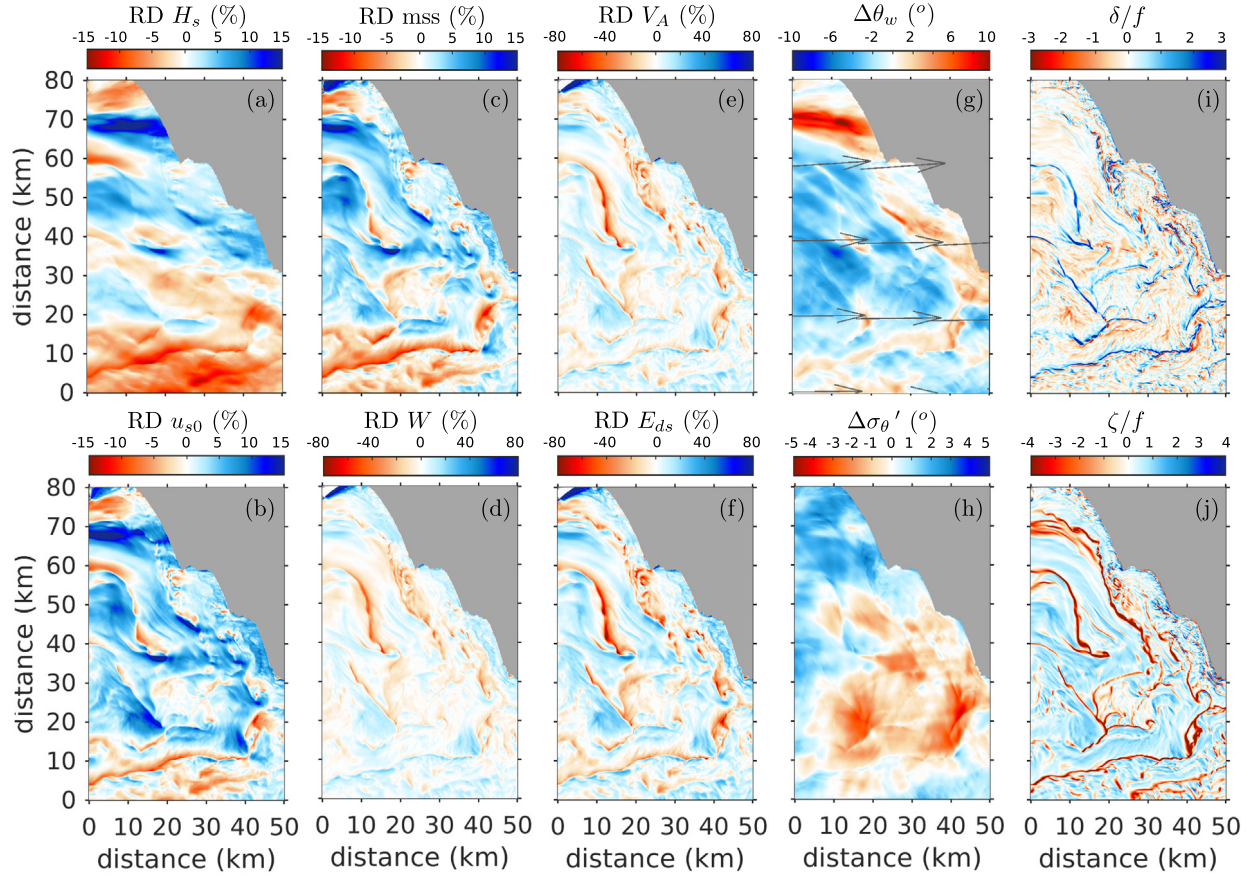


Fig. 9. Same as in Fig. 8 for the L3 configuration.

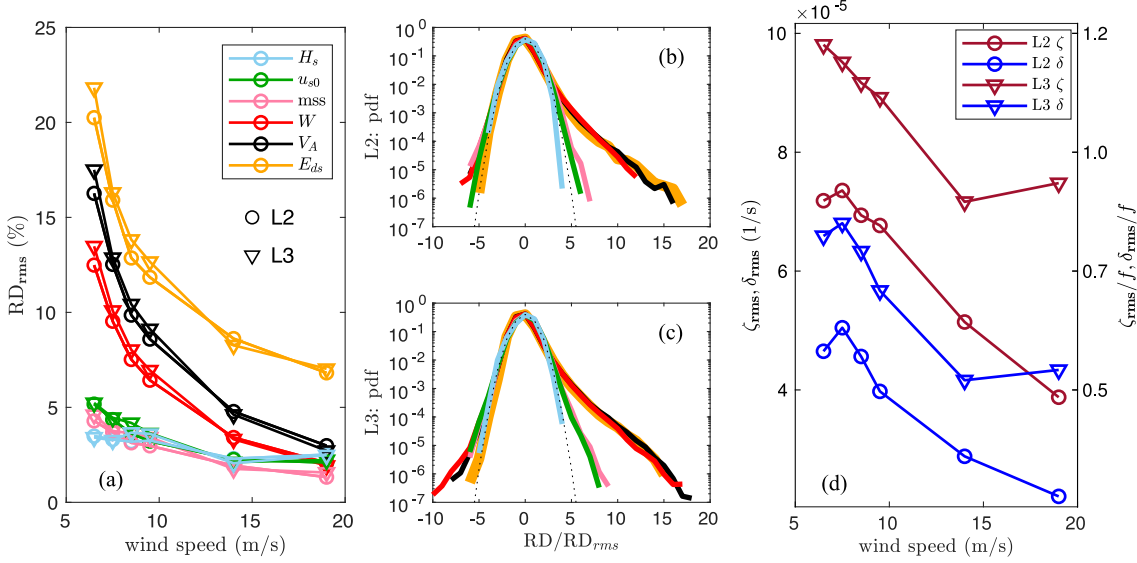


Fig. 10. (a) Root-mean-square (rms) relative difference RD_{rms} between solutions forced by winds and currents (CEW) and wind-only (WND) showing H_s , u_{s0} , mss, W , V_A , and E_{ds} , color-coded as indicated in the legend. The L2 and L3 solutions are shown with circles and triangles, respectively. The corresponding probability density functions (pdfs) are shown in panels (b) and (c), for L2 and L3, respectively. The black dotted lines are the Gaussian distribution. The root-mean-square values of divergence δ and vorticity ζ against wind speed are shown in panel (d). The rms values and distributions were computed from data between 12/26/2006 and 1/1/2007 within the white dotted box in the open ocean outside the Southern California Bight, shown in Fig. 1a.

3.5. Seasonal variability and scaling

In this subsection, the model differences due to CEW in the open ocean are further analyzed comparing the one-month-long L2 winter and spring solutions, which are plotted against wind speed in Fig. 12.

The RD rms values are approximately 2 times larger for the winter solution compared to the spring for all variables. The rms surface vorticity and divergence are also larger in the winter compared to the spring but only by about 20%. Similarly, the spectrally weighted wave period (not shown) is on average 11 s in the winter compared to 9 s

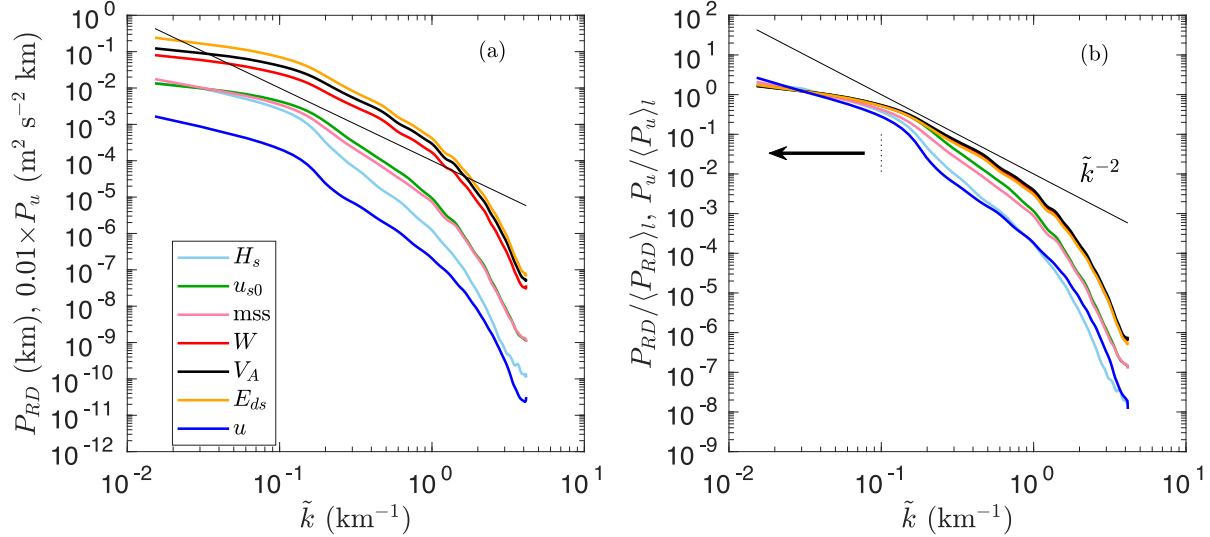


Fig. 11. (a) Wavenumber spectra of relative differences (RD) between CEW and WND L3 solutions for H_s , u_{s0} , mss, W , V_A , and E_{ds} , color-coded as indicated in the legend. The variable \tilde{k} denotes the wavenumber of the spectra shown here to differentiate from that of the wave spectrum. For reference, the corresponding spectrum of the surface current speed is shown in blue scaled by a factor of 0.01. (b) Spectra are normalized by the linear spectrum average for $\tilde{k} < 0.1 \text{ km}^{-1}$ or scales greater than 10 km as indicated by the black arrow, see also definition in Eq. (22). Spectra were computed along the longer axis in the middle of the white dotted box in Fig. 1a and averaged for the period between 12/26/2006 and 1/1/2007.

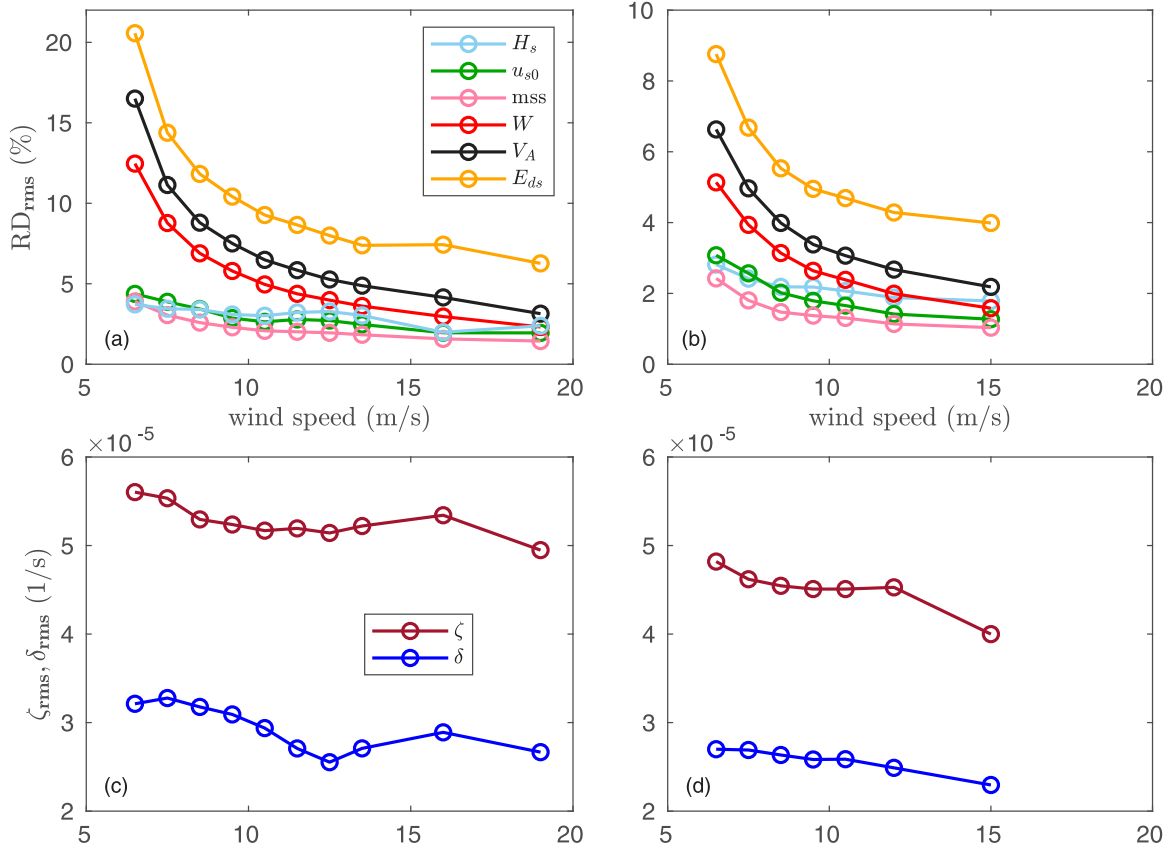


Fig. 12. Root-mean-square relative differences between wave solutions forced by winds and currents and wind-only for the one-month long L2 winter (a) and spring (b) solutions, with the corresponding surface rms vorticity (c) and rms divergence (d). The statistics were computed from data within the white dashed box in Fig. 1a.

in spring. In other words as expected, the rms relative differences due to CEW are larger for the winter solution when the current gradients are stronger and mean wave period is larger (Phillips, 1984). Here, the model differences due to CEW across seasons and model resolution are characterized with an empirical scaling as described below.

Phillips (1984) introduced a non-dimensional parameter controlling the spectral response of wind forced waves to current variations defined as the product vI , where $v = U_o L^{-1} T$, and $I = g^2 T^2 (2\pi u_*)^{-2}$, with $U_o L^{-1}$ representing the current gradients, T the wave period, and u_* the air-side friction velocity. We use a dimensionless function $\xi v^N I^M$

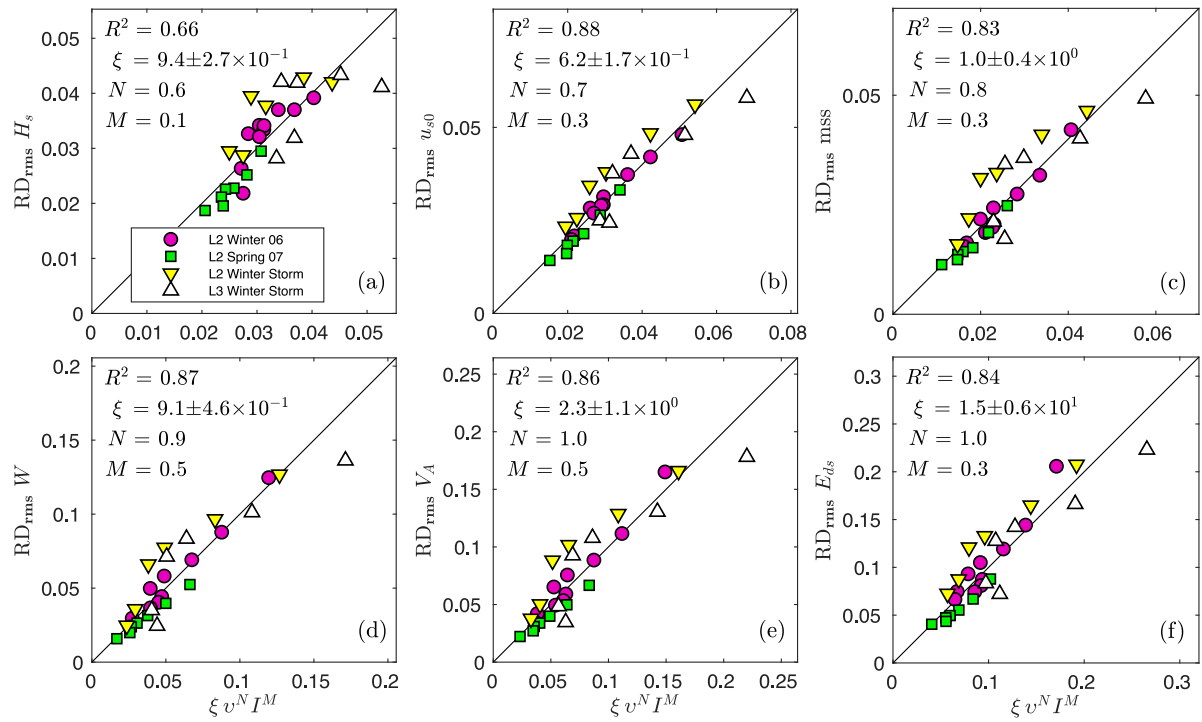


Fig. 13. Root-mean-square relative difference against the non-dimensional scaling $\xi v^N I^M$, where $v = (\delta_{rms}^2 + \zeta_{rms}^2)^{1/2} \bar{T}_{0,-1}$ and $I = (\frac{g}{2\pi} \frac{\bar{T}_{0,-1}}{u_*})^2$, with $\bar{T}_{0,-1}$ is the spectrally weighted wave period, and u_* is the air-side friction velocity. The non-dimensional coefficients ξ , N , and M were obtained by least-squares fitting and are shown in each panel along with the fraction of variance explained (R^2). The L2 winter and spring data correspond to the bin-averages from one-month long solutions shown in Fig. 12 calculated within the white dashed box in Fig. 1a. The data for winter storm are those from Fig. 10 calculated within the white dotted box in Fig. 1 overlapping with both the L2 and L3 configurations.

to scale the rms differences due to CEW using the resolved friction velocity u_* , the spectrally weighted mean period $T_{0,-1}$, and rms vorticity (ζ_{rms}) and divergence (δ_{rms}), such that $v = (\delta_{rms}^2 + \zeta_{rms}^2)^{1/2} \bar{T}_{0,-1}$ and $I = (\frac{g}{2\pi} \frac{\bar{T}_{0,-1}}{u_*})^2$. The exponents N , M , and the dimensionless factor ξ were determined through least-squares fitting against the rms relative differences due to CEW for the L2 winter and spring solutions, and the overlapping L2 and L3 solutions previously analyzed covering a week-long period including the largest winter storm. Fig. 13 shows the RD rms values for the different variables against the empirical scaling along with the best-fit coefficients and the fraction of variance explained (R^2). The R^2 values are 0.83 or larger for all the variables except for H_s with $R^2 = 0.66$. The best-fit coefficients $\xi = 0.9 \pm 0.2$, 0.6 ± 0.2 , 1.0 ± 0.4 , 0.9 ± 0.5 , 2.3 ± 1.0 , and 15 ± 6 , and $N = 0.6$, 0.7 , 0.8 , 0.9 , 1.0 , and 1.0 , and $M = 0.1$, 0.3 , 0.3 , 0.5 , 0.5 , and 0.3 for $RD_{rms} H_s$, u_{s0} , mss , W , V_A , and E_{ds} , respectively.

In an attempt to improve the R^2 value of the rms relative differences of H_s , we considered the surface current projected onto the mean wave direction according to $u_w = u \cos(\theta_w) + v \sin(\theta_w)$, decomposed into a mean a fluctuating part as $u_w = \langle u_w \rangle + u'_w$. The best correlation for H_s was found against a scaling of the form $\xi v^N \chi^P$, with $\chi = \langle u'_w^2 \rangle / (\langle u^2 \rangle + \langle v^2 \rangle)$ with $\xi = 3.5 \pm 0.8$, $N = 0.6$, and $P = 0.3$ giving $R^2 = 0.8$. All other variables give comparable R^2 values as for the original scaling dependent on the wind forcing, in part because of a strong correlation between the mean square current and the friction velocity ($R^2 = 0.8$).

As suggested by one reviewer, other scalings based on polynomials formed with the same nondimensional variables were tested and found to give similar R^2 coefficients but the power-law scalings are preferred because they tend to zero as the current gradients go to zero. Also, other measures of the wave period (e.g., inverse spectrally weighted wave frequency) were tested and found to give qualitatively similar results but with equal or lower R^2 values. Similarly, using the vorticity or divergence alone for the velocity gradient scaling results in differences of R^2 of 0.02 or smaller for all the variables.

4. Discussion

4.1. Current induced refraction in the Santa Barbara channel

Regional wave models in Southern California without external forcing have reported relatively large errors in the Santa Barbara Channel (O'Reilly and Guza, 1993, 1998; O'Reilly et al., 2016; Crosby et al., 2016), which have been attributed not only to the reflection of wave energy from the Channel Islands (O'Reilly et al., 1999), but also due to forcing by currents and winds (Crosby et al., 2016). In this study, the differences in H_s between runs with and without CEW were shown to be generally small but occasionally large at the Goleta buoy during low winds, for example with H_s increasing by 60% due to CEW on 12/13 in good agreement with the observations. The model runs presented did not include reflections at the coastline. Additional runs were carried out including reflections at the shoreline with source term function by Arduhin and Roland (2012). As expected, the results did not significantly affect the significant wave height, with changes of less than 15%, mostly affecting the directional spreading at all buoy locations.

The effects of currents for the wave field in the Santa Barbara Channel are further analyzed in Fig. 14 comparing snapshots of H_s within the Santa Barbara Channel from the solution forced by winds (a) and that forced by winds and currents (b) on 12/13 at 00:00 UTC. The relative difference along with surface current vectors and wave propagation rays are shown in 14c,d, respectively. Rays were computed for the peak wave period (15 s) and direction (298° from true north — energy from) accounting for the refraction due to bathymetry (green) and both bathymetry and surface current gradients (black) according to Mathiesen (1987). The circulation in the Santa Barbara Channel and in particular the Santa Barbara Eddy result in pronounced effects for the wave energy. The areas with relative H_s differences within the channel reaching values of 80% overlap with the areas where wave propagation rays converge. The amplification of the wave energy due to currents along the mainland coast is relatively large on the eastern

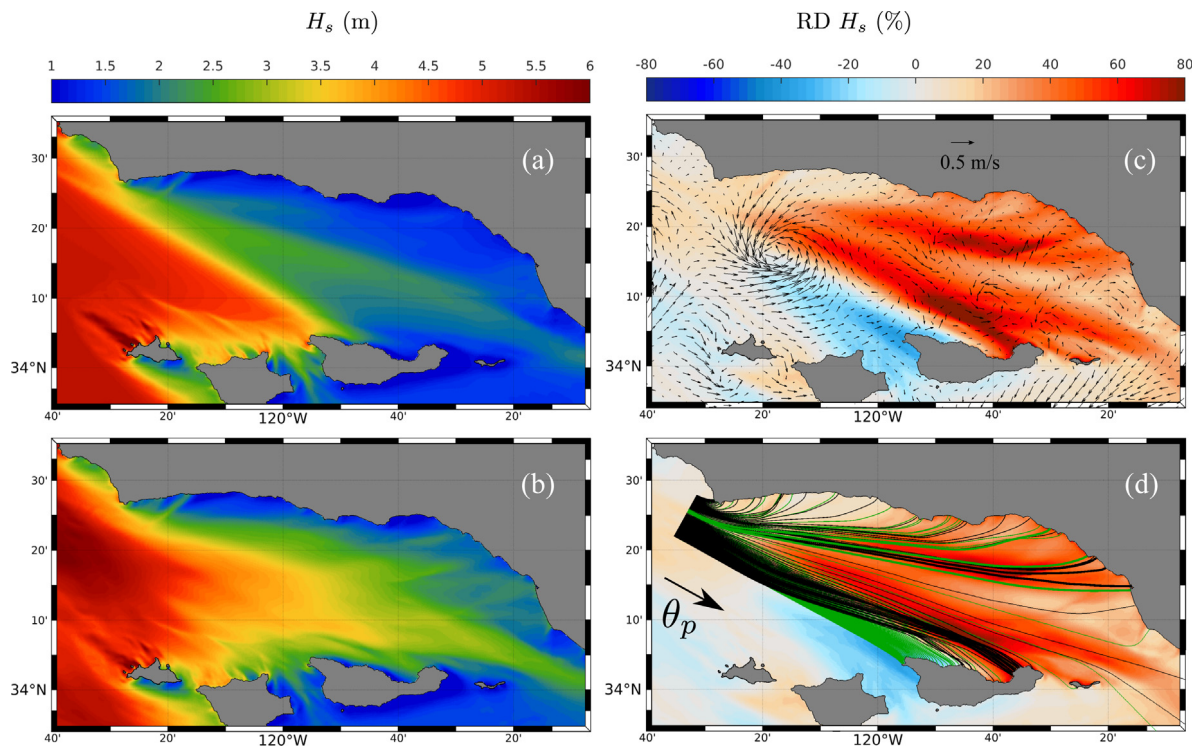


Fig. 14. Significant wave height during a relatively large wave event and low winds ($U_{10} \sim 5$ m/s) within the Santa Barbara Channel on 12/13/2006 00:00 (UTC) for the L2 solution forced by wind (a) and CEW (b). Relative difference is shown with surface currents subsampled by a factor of 10 in (c) and corresponding wave refraction rays in (d). Wave propagation rays were calculated for the peak period of 15 s and peak direction (θ_p) at 298° from the North accounting for both bottom-induced and current-induced refraction (black) and bottom refraction only (green). The thicker lines highlight three initially adjacent rays that converge due to currents and otherwise would diverge.

side reaching values up to 50%. The effects of the currents on the waves in the Santa Barbara Channel and other sheltered areas could be further explored more accurately with WW3 forced by measured currents from High-Frequency radars and their uncertainty (Emery and Washburn, 2019) and an array of low-cost buoys (Raghukumar et al., 2019) or airborne LIDAR measurements (Romero and Melville, 2010a; Romero et al., 2017).

4.2. CEW contributions and relative wind

As described earlier, CEW within the WW3 framework comes in from advection (A), refraction (R), and direct forcing (D) by currents corresponding to terms 2–4 in Eq. (1). However, surface currents can also affect the wind input (S_{in}) through the effective or relative wind, which is the vector difference between the surface wind and the current. Here the different contributions to CEW are analyzed with control runs. Specifically, the L2 configuration in deep-water during the last week of December 2006 comparing solutions with different forcing. The rms relative differences for the different variables are shown in Fig. 15, color-coded according to the enabled physics as indicated in the legend. The solution only accounting for advection by currents shows the lowest rms RD values for all the variables. Refraction is most significant for H_s , followed by u_{s0} and mss, being least significant for the breaking variables. The direct forcing by current gradients and relative winds are significant for all the variables except for H_s . The relative winds on average increase the rms relative differences by 30% for the breaking and 15% for u_{s0} and mss.

The dominance of refraction for the modulation of the total energy or H_s is consistent with the work by Bôas and Young (2020). Both Smit and Janssen (2019) and Bôas and Young (2020) investigated wave diffusion due to refraction and wave action conservation as the wave field propagates through submesoscale and mesoscale turbulent fields over relatively long distances (100's km). The diffusion and energy decay rates are directly tied to the directional spreading. In

our solutions, CEW increases the directional spreading on average by $0.9^\circ \pm 0.2^\circ$ with a directional spreading variability of $\pm 3^\circ$ and wave direction variability within $\pm 5^\circ$ at the 95% confidence interval across model resolutions and seasons with a weak inverse dependence on the wind forcing. These results are expected to be sensitive to the nonlinear energy fluxes (S_{nl}), for example the DIA compared to “exact” computations (e.g., Tracy and Resio, 1982; van Vledder, 2006), but the latter is not yet computationally tractable for regional models.

In the context of current and depth variations at scales of the order of the wavelength of the longer waves O(100 m), the WKB approximation is not valid and coherent interferences become important. These effects are phase-dependent but can be explored with phase average spectral models within the framework of Smit and Janssen (2013) and Akrish et al. (2020). Also, feedback due to WEC can be significant on submesoscale processes, such as fronts and filaments (Suzuki et al., 2016; McWilliams, 2018), which will in turn affect CEW. Future work will explore both CEW and WEC with a fully-coupled model configuration.

4.3. Wave-breaking variability and feedbacks at submesoscales

The results show that CEW is significant for breaking at scales of order 1 km and smaller which is qualitatively consistent with the measurements by Romero et al. (2017). The variability of wave breaking is strongly coupled to sharp surface current gradients where the flow is strongly three-dimensional. This implies that air-sea fluxes, for example gas transfer, may be enhanced due to wave-current interactions over areas with increased submesoscale activity like the Southern Ocean. However, both ROMS and WW3 at the sub-kilometer resolutions are computationally expensive, not realistically feasible for global applications. In addition to the coupling between wave breaking and surface current variability, the statistical distributions for the wave-breaking variables are strongly skewed with larger positive values which may result in potentially important effects on air-sea fluxes

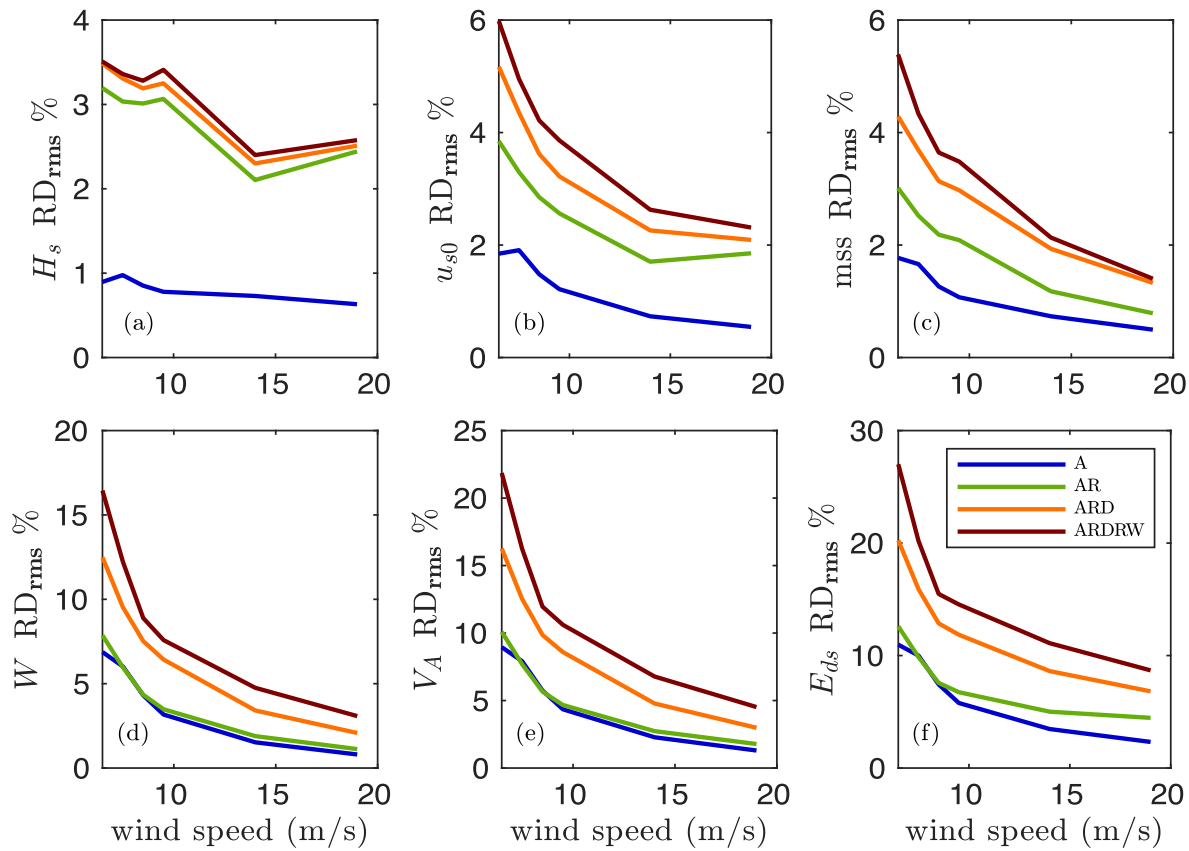


Fig. 15. Root-mean-square relative differences between wave solutions forced by winds and currents (CEW) and wind-only. The physics used for each CEW solution are indicated in the legend and labeled as: advection (A), refraction (R), direct forcing by the current gradients (D) and relative winds (RW). The rms values were computed from data for the period of the last week of December 2006 as in Fig. 10 within the white dashed box in Fig. 1.

due to wave breaking globally. The pdfs of the model solutions with and without CEW combined with the empirical scaling of the rms differences could be used for stochastic analysis of the impacts of CEW at global scales.

The relatively larger impact of CEW on the energy dissipation and rate of air entrainment compared to the whitecap coverage, besides the fact that they depend on different moments of Λ , is due to the additional nonlinear dependence on $B(k)$ in Eqs. (18) and (9). Taking the results in Romero (2019) from idealized runs for developing waves with constant winds, we find that $V_A \sim W^{1.25}$ and $E_{ds} \sim W^{1.66}$. These relationships exhibit substantial variability due to wave age that is not accounted for with these simple power-laws. Nevertheless, the exponents imply that the relative differences of V_A and E_{ds} due to CEW compared to those of W would be 1.25 and 1.66 times larger, respectively. These factors are qualitatively consistent with the enhancement of RD_{rms} in Figs. 10a and 12a,b for V_A and E_{ds} compared to W .

The results showed that CEW is significant for wave breaking at low winds ($< 10 \text{ m/s}$), which is representative of global mean values (Semedo et al., 2011). In fact, the observed average wind speed over the ocean is about 7 m/s (Freilich and Challenor, 1994; Rodriguez, 2018). Several parameterizations in the literature of wave breaking and related air-sea fluxes depend on wind speed or friction velocity, and wave age, or H_s (Brumer et al., 2017a,b; Deike and Melville, 2018; Reichl and Deike, 2020). But as shown here and by Romero et al. (2017), the wave-breaking variability due to currents at scales of 1 km or smaller cannot be accounted for through H_s . Instead, a measure of the current gradients at scales of less than 1 km, along with the friction velocity and mean wave period may lead to improved parameterizations of wave breaking and related air-sea fluxes.

In the context of upper-ocean processes, the modeling study by Gerbi et al. (2013) investigated the effect of the turbulent kinetic

energy flux induced by wave breaking on the dynamics of buoyant plumes. Their results show that wave breaking induced mixing results in deeper and narrower plumes with weaker vertical gradients of temperature and salinity affecting the plume evolution. In that study, wave breaking was parameterized as a function of the wind stress not accounting for CEW. As shown here, the wave breaking is strongly modulated at submesoscales due to CEW which may lead to nontrivial effects on the evolution and dynamics of fronts and plumes. Similarly, the ocean-side stress explicitly accounting wave breaking will be highly structured due to CEW and correlated with submesoscale flow structures such as fronts, filaments, and eddies. More generally, heterogeneous wave fields due to CEW will make heterogeneous wave effects on currents (WEC) through Stokes drift, vertical mixing, and surface stress. Moreover, fully coupled ocean-wave-atmospheric models may also affect the eddy killer effect in which the feedback acts as a sink of energy in both the ocean and the atmosphere due to the coupling (Renault et al., 2016).

5. Conclusions

We presented a modeling study of current effects on waves with a realistic nested configuration in Southern California at high resolutions, 270 m (L2) and 100 m (L3). The analysis compared two one-month-long periods during the winter (2006) and spring (2007) with relatively active wave climates. Solutions without external forcing were used to assess model performance regarding the importance of the winds and currents, particularly within sheltered areas. Wind forcing can significantly reduce model biases in the Southern California Bight, particularly in the Santa Barbara Channel. In low wind conditions, the significant wave height in the Santa Barbara Channel can increase by up to 50% along the main coast of Santa Barbara and by up to 80% within the Santa Barbara Channel due to current-induced refraction.

In open ocean, CEW is most significant at low winds and increases with model resolution due to increased submesoscale activity. L2 Solutions forced by currents compared to those without in 10 m/s winds give differences of $\pm 12\%$ for H_s , Surface Stokes drift and mss, and can reach 50% or more for the whitecap coverage W , and the volume of entrained air V_A and energy dissipation E_{ds} by breaking waves. For the higher resolution solution (L3) these values become 15% and 70% or larger, respectively. CEW on average increases the directional spreading by $0.9^\circ \pm 0.2^\circ$ with $\pm 3^\circ$ variability and modulates the mean wave direction within $\pm 5^\circ$. A statistical analysis of the model differences due to CEW when normalized by the rms variability result in approximately self-similar distributions independent of model resolution, with H_s well represented by the Gaussian distribution, Stokes drift and mss symmetric with finite excess kurtosis, and the wave-breaking variables (W , V_A and E_{ds}) positively skewed with finite excess kurtosis. CEW is stronger for the winter solution compared to the spring (Fig. 13). An empirical scaling based on the rms current gradients, air-side friction velocity and mean wavelength explain most of the variability due to CEW across the two seasons and the two model resolutions considered (Fig. 13) with $R^2 = 0.8$ or larger except for H_s with $R^2 = 0.66$.

Wavenumber spectra of model differences due to CEW are proportional to the spectrum of the surface current magnitude. However, the difference spectrum for H_s decreases faster with decreasing scale than the current spectrum for scales smaller than 1 km. In contrast the surface Stokes drift, mss, and wave-breaking variables decay less steeply with decreasing scale than the current spectrum across the range of scales analyzed (10's km to 100's m), with the largest variability compared to the current spectrum at small scales for the wave-breaking variables considered, namely whitecap coverage, air-entrainment rate, and energy dissipation rate. Future work will characterize wave effects on currents (WEC) due to both conservative and non-conservative effects within the framework of McWilliams et al. (2004) and Uchiyama et al. (2010) with our testbed including higher resolutions better resolving nearshore processes. Other efforts will investigate the impact of wave-current interactions on CO₂ fluxes.

CRediT authorship contribution statement

Leonel Romero: Conceptualization, Methodology, Validation, Visualization, Writing - original draft. **Delphine Hypolite:** Writing - review & editing. **James C. McWilliams:** Writing - review & editing.

Declaration of competing interest

The authors declare that they have no known competing financial interests or personal relationships that could have appeared to influence the work reported in this paper.

Acknowledgments

This work used computer resources from DoD HPC Modernization Program, NCAR's Computational and Information Systems Lab (CISL), and the Extreme Science and Engineering Discovery Environment (XSEDE) #TG-OCE030000N. LR was supported by grants from the Office of Naval Research (ONR) N00014-16-1-2936 and the National Science Foundation (NSF) OCE-1924686. JCM acknowledges support from Calif. Natural Resources Agency C0100400, the National Oceanic and Atmospheric Administration (NOAA) 0471-2015:04, NSF OCE-1355970, and ONR N00014-15-1-2645. We appreciate the feedback from anonymous reviewers which helped to improve this work. LR dedicates this paper to the memory of Ken Melville.

References

- Akrish, G., Smit, P., Zijlema, M., Reniers, A., 2020. Modelling statistical wave interferences over shear currents. *J. Fluid Mech.* 891, A2.
- Ardhuin, F., Gille, S.T., Menemenlis, D., Rocha, C.B., Raschke, N., Chapron, B., Gula, J., Molesmaker, J., 2017. Small-scale open ocean currents have large effects on wind wave heights. *J. Geophys. Res.: Oceans* 122 (6), 4500–4517.
- Ardhuin, F., O'Reilly, W.C., Herbers, T.H.C., Jessen, P.F., 2003. Swell transformation across the continental shelf. Part I: Attenuation and directional broadening. *J. Phys. Ocean.* 33 (9), 1921–1939.
- Ardhuin, F., Rogers, E., Babanin, A.V., Filipot, J.-F., Magne, R., Roland, A., van der Westhuysen, A., Queffulou, P., Lefevre, J.-M., Aouf, L., Collard, F., 2010. Semimipirical dissipation source functions for ocean waves. Part I: Definition, calibration, and validation. *J. Phys. Ocean.* 40 (9), 1917–1941.
- Ardhuin, F., Roland, A., 2012. Coastal wave reflection, directional spread, and seismoacoustic noise sources. *J. Geophys. Res.: Oceans* 117 (6), 1–16.
- Becker, J.J., Sandwell, D.T., Smith, W.H.F., Braud, J., 2009. Global bathymetry and elevation data at 30 arc seconds resolution : SRTM30 _ PLUS. *Mar. Geod.* 32, 355–371.
- Benoit, M., 1992. Practical comparative performance survey of methods used for estimating directional wave spectra from heave pitch roll data. In: Coastal Engineering Proceedings 23. Venice, Italy. pp. 162–175.
- Bóas, A.B., Young, W.R., 2020. Directional diffusion of surface gravity wave action by ocean macroturbulence. *J. Fluid Mech.* 1–12.
- Brumer, S.E., Zappa, C.J., Blomquist, B.W., Fairall, C.W., Cifuentes-Lorenzen, A., Edson, J.B., Brooks, I.M., Huebert, B.J., 2017a. Wave-related Reynolds number parameterizations of CO₂ and DMS transfer velocities. *Geophys. Res. Lett.* 44 (19), 9865–9875.
- Brumer, S.E., Zappa, C.J., Brooks, I.M., Tamura, H., Brown, S.M., Blomquist, B.W., Fairall, C.W., Cifuentes-Lorenzen, A., 2017b. Whitecap coverage dependence on wind and wave statistics as observed during SO GasEx and HiWinGS. *J. Phys. Ocean.* 47 (9), 2211–2235.
- Buijsman, M.C., Uchiyama, Y., McWilliams, J.C., Hill-Lindsay, C.R., 2012. Modeling semidiurnal internal tide variability in the Southern California Bight. *J. Phys. Ocean.* 42 (1), 62–77.
- Cao, Y., Dong, C., Uchiyama, Y., Wang, J., Yin, X., 2018. Multiple-scale variations of wind-generated waves in the Southern California Bight. *J. Geophys. Res.: Oceans* 123 (12), 9340–9356.
- Capon, J., 1969. High-resolution frequency-wavenumber spectrum analysis. *Proc. IEEE* 57 (8), 1408–1418.
- Carton, J.A., Giese, B.S., 2008. A reanalysis of ocean climate using simple ocean data assimilation (SODA). *Mon. Weather Rev.* 136 (8), 2999–3017.
- Cox, C., Munk, W., 1954. Statistics of the sea surface derived from sun glitter. *J. Mar. Res.* 13, 198–227.
- Crosby, S.C., O'Reilly, W.C., Guza, R.T., 2016. Modeling long-period swell in Southern California: Practical boundary conditions from buoy observations and global wave model predictions. *J. Atmos. Ocean Technol.* 33 (8), 1673–1690.
- Dauhajre, D.P., McWilliams, J.C., Renault, L., 2019. Nearshore Lagrangian connectivity: Submesoscale influence and resolution sensitivity. *J. Geophys. Res.: Oceans* 124, 5180–5204.
- Deike, L., Lenain, L., Melville, W.K., 2017. Air entrainment by breaking waves. *Geophys. Res. Lett.* 44 (8), 3779–3787.
- Deike, L., Melville, W.K., 2018. Gas transfer by breaking waves. *Geophys. Res. Lett.* 45 (19), 10,482–10,492.
- Emery, B., Washburn, L., 2019. Uncertainty estimates for SeaSonde HF radar ocean current observations. *J. Atmos. Ocean Technol.* 36 (2), 231–247.
- Freilich, M.H., Challenor, P.G., 1994. A new approach for determining fully empirical altimeter wind speed model functions. *J. Geophys. Res.* 99 (C12), 25051–25062.
- Gerbi, G.P., Chant, R.J., Wilkin, J.L., 2013. Breaking surface wave effects on river plume dynamics during upwelling-favorable winds. *J. Phys. Ocean.* 43 (9), 1959–1980.
- Hasselmann, S., Hasselmann, K., 1985. Computations and parameterizations of the nonlinear energy transfer in a gravity-wave spectrum. Part II: Parameterizations of the nonlinear energy transfer for application in wave models. *J. Phys. Ocean.* 15, 1378–1391.
- Hjelmervik, K.B., Trulsen, K., 2009. Freak wave statistics on collinear currents. *J. Fluid Mech.* 637, 267–284.
- Janssen, P.A.E.M., 1989. Wave-induced stress and drag of air flow over sea waves. *J. Phys. Ocean.* 19, 745–754.
- Janssen, P.A.E.M., 1991. Quasi-linear theory of wind-wave generation applied to wave forecasting. *J. Phys. Ocean.* 21, 1631–1642.
- Janssen, T.T., Herbers, T.H.C., 2009. Nonlinear wave statistics in a focal zone. *J. Phys. Ocean.* 39 (8), 1948–1964.
- Kleiss, J.M., Melville, W.K., 2010. Observations of wave breaking kinematics in fetch-limited seas. *J. Phys. Ocean.* 40, 2575–2604.
- Kudryavtsev, V., Yurovskaya, M., Chapron, B., Collard, F., Donlon, C., 2017. Sun glitter imagery of surface waves. Part 2: Waves transformation on ocean currents. *J. Geophys. Res.: Oceans* 122 (2), 1384–1399.
- Kuik, A.J., van Vledder, G.P., Holthuijsen, L.H., 1988. A method for the routine analysis of pitch-and-roll buoy wave data. *J. Phys. Ocean.* 18 (7), 1020–1034.

- Kumar, N., Suanda, S.H., Colosi, J.A., Haas, K., Di Lorenzo, E., Miller, A.J., Edwards, C.A., 2019. Coastal semidiurnal internal tidal incoherence in the Santa Maria Basin, California: Observations and model simulations. *J. Geophys. Res.: Oceans* 124 (7), 5158–5179.
- Lenain, L., Melville, W.K., 2017. Measurements of the directional spectrum across the equilibrium saturation ranges of wind-generated surface waves. *J. Phys. Ocean.* 47, 2123–2138.
- Liu, Q., Rogers, W.E., Babanin, A.V., Young, I.R., Romero, L., Zieger, S., Qiao, F., Guan, C., 2019. Observation-based source terms in the third-generation wave model WAVEWATCH III: Updates and verification. *J. Phys. Ocean.* 49 (2), 489–517.
- Lygre, A., Krogstad, H.E., 1986. Maximum entropy estimation of the directional distribution in ocean wave spectra. *J. Phys. Ocean.* 16 (12), 2052–2060.
- Mathiesen, M., 1987. Wave refraction by a current whirl. *J. Geophys. Res.* 92 (C4), 3905–3912.
- McWilliams, J.C., 2016. Submesoscale currents in the ocean. *Proc. R. Soc. Lond. Ser. A Math. Phys. Eng. Sci.* 472, 20160117.
- McWilliams, J.C., 2018. Surface wave effects on submesoscale fronts and filaments. *J. Fluid Mech.* 843, 479–517.
- McWilliams, J.C., Restrepo, J.M., Lane, E.M., 2004. An asymptotic theory for the interaction of waves and currents in coastal waters. *J. Fluid Mech.* 511, 135–178.
- Onorato, M., Proment, D., Toffoli, A., 2011. Triggering rogue waves in opposing currents. *Phys. Rev. Lett.* 107 (18), 1–5.
- O'Reilly, W.C., Guza, R.T., 1993. A comparison of two spectral wave models in the Southern California Bight. *Coast. Eng.* 19 (3–4), 263–282.
- O'Reilly, W.C., Guza, R.T., 1998. Assimilating coastal wave observations in regional swell predictions. Part I: Inverse methods. *J. Phys. Ocean.* 28 (4), 679–691.
- O'Reilly, W.C., Guza, R.T., Seymour, R.J., 1999. Wave prediction in the santa barbara channel. In: Proceedings of the 5th California Islands Symposium. Santa Barbara, CA, 29 March–1 April. pp. 76–80.
- O'Reilly, W.C., Olfe, C.B., Thomas, J., Seymour, R.J., Guza, R.T., 2016. The california coastal wave monitoring and prediction system. *Coast. Eng.* 116, 118–132.
- Phillips, O.M., 1984. On the response of short ocean wave components at a fixed wavenumber to ocean current variations. *J. Phys. Oceanogr.* 14 (September), 1425–1433.
- Phillips, O.M., 1985. Spectral and statistical properties of the equilibrium range in wind-generated gravity waves. *J. Fluid Mech.* 156, 505–531.
- Ponte, A.L., Klein, P., 2015. Incoherent signature of internal tides on sea level in idealized numerical simulations. *Geophys. Res. Lett.* 42 (5), 1520–1526.
- Quilfen, Y., Chapron, B., 2019. Ocean surface wave-current signatures from satellite altimeter measurements. *Geophys. Res. Lett.* 46 (1), 253–261.
- Quilfen, Y., Yurovskaya, M., Chapron, B., Arduhin, F., 2018. Storm waves focusing and steepening in the Agulhas current: Satellite observations and modeling. *Remote Sens. Environ.* 216 (July), 561–571.
- Raghukumar, K., Chang, G., Spada, F., Jones, C., Janssen, T., Gans, A., 2019. Performance characteristics of “spotter,” a newly developed real-time wave measurement buoy. *J. Atmos. Ocean Technol.* 36 (6), 1127–1141.
- Rascle, N., Chapron, B., Ponte, A., Arduhin, F., Klein, P., 2014. Surface roughness imaging of currents shows divergence and strain in the wind direction. *J. Phys. Ocean.* 44 (8), 2153–2163.
- Rascle, N., Molemaker, J., Marié, L., Nouguier, F., Chapron, B., Lund, B., Mouche, A., 2017. Intense deformation field at oceanic front inferred from directional sea surface roughness observations. *Geophys. Res. Lett.* 44 (11), 5599–5608.
- Rascle, N., Nouguier, F., Chapron, B., Mouche, A., Ponte, A., 2016. Surface roughness changes by finescale current gradients: Properties at multiple azimuth view angles. *J. Phys. Ocean.* 46 (12), 3681–3694.
- Reichl, B.G., Deike, L., 2020. Contribution of Sea-State Dependent Bubbles to Air-Sea Carbon Dioxide Fluxes. *Geophysical Research Letters* 47 (9), e2020GL087267.
- Renault, L., Molemaker, M.J., Mcwilliams, J.C., Shchepetkin, A.F., Lemarié, F., Chelton, D., Illig, S., Hall, A., 2016. Modulation of wind work by oceanic current interaction with the atmosphere. *J. Phys. Ocean.* 46 (6), 1685–1704.
- Resio, D.T., Long, C.E., Vincent, C.L., 2004. Equilibrium-range constant in wind-generated wave spectra. *J. Geophys. Res.* 109 (C1), C01018.
- Rodriguez, E., 2018. On the optimal design of doppler scatterometers. *Remote Sens.* 10 (11), 1765.
- Rogers, W.E., Kaihatu, J.M., Hsu, L., Jensen, R.E., Dykes, J.D., Holland, K.T., 2007. Forecasting and hindcasting waves with the SWAN model in the Southern California Bight. *Coast. Eng.* 54 (1), 1–15.
- Romero, L., 2019. Distribution of surface wave breaking fronts. *Geophys. Res. Lett.* 46 (17–18), 10463–10474.
- Romero, L., Lenain, L., Melville, W.K., 2017. Observations of surface wave-current interaction. *J. Phys. Ocean.* 47 (3), 615–632.
- Romero, L., Melville, W.K., 2010a. Airborne observations of fetch-limited waves in the gulf of tehuantepec. *J. Phys. Ocean.* 40 (3), 441–465.
- Romero, L., Melville, W.K., Kleiss, J.M., 2012. Spectral energy dissipation due to surface wave breaking. *J. Phys. Ocean.* 42 (9), 1421–1444.
- Romero, L., Siegel, D.A., McWilliams, J.C., Uchiyama, Y., Jones, C., 2016. Characterizing storm water dispersion and dilution from small coastal streams. *J. Geophys. Res.: Oceans* 121 (6), In review.
- Romero, L., Uchiyama, Y., Ohlmann, J.C., McWilliams, J.C., Siegel, D.A., 2013. Simulations of nearshore particle-pair dispersion in Southern California. *J. Phys. Ocean.* 43 (9), 1862–1879.
- Semedo, A., Sušelj, K., Rutgersson, A., Sterl, A., 2011. A global view on the wind sea and swell climate and variability from ERA-40. *J. Clim.* 24 (5), 1461–1479.
- Smit, P.B., Janssen, T.T., 2013. The evolution of inhomogeneous wave statistics through a variable medium. *J. Phys. Ocean.* 43 (8), 1741–1758.
- Smit, P.B., Janssen, T.T., 2019. Swell propagation through submesoscale turbulence. *J. Phys. Ocean.* 49 (10), 2615–2630.
- Stewart, R.H., Joy, J.W., 1974. HF radio measurements of ocean surface currents. *Deep-Sea Res.* 21, 1039–1049.
- Sutherland, P., Melville, W.K., 2013. Field measurements and scaling of ocean surface wave-breaking statistics. *Geophys. Res. Lett.* 40 (12), 3074–3079.
- Suzuki, N., Fox-Kemper, B., Hamlington, P.E., Van Roekel, L.P., 2016. Surface waves affect frontogenesis. *J. Geophys. Res.: Oceans* 121 (5), 3597–3624.
- The WAVEWATCH III Development Group [WW3DG], 2016. User Manual and System Documentation of WAVEWATCH III Version 5.16, Vol. 276. Tech. Note 329, NOAA/NWS/NCEP/MMAB, College Park, MD, USA, Technical note, MMAB Contribution, 326 pp. + Appendices.
- Tolman, H.L., 2002. Alleviating the garden sprinkler effect in wind wave models. *Ocean Model.* 4 (3–4), 269–289.
- Tolman, H.L., Booij, N., 1998. Modeling wind waves using wavenumber-direction spectra and a variable wavenumber grid. *Glob. Atmos. Ocean Syst.* 6, 295–309.
- Tracy, B., Resio, D.T., 1982. Theory and Calculation of the Nonlinear Energy Transfer between Sea Waves in Deep Water. Technical Report Hydraulics Lab WIS Technical Report 11, Hydraulics Lab, WIS Technical Report 11. US Army Engineer Waterways Experiment Station, Vicksburg, Mississippi, USA, p. 50.
- Uchiyama, Y., Idica, E.Y., McWilliams, J.C., Stolzenbach, K.D., 2014. Wastewater effluent dispersal in Southern California bays. *Cont. Shelf Res.* 76, 36–53.
- Uchiyama, Y., McWilliams, J.C., Shchepetkin, A.F., 2010. Wave-current interaction in an oceanic circulation model with a vortex-force formalism: Application to the surf zone. *Ocean Model.* 34 (1–2), 16–35.
- Van Haren, H., 2004. Incoherent internal tidal currents in the deep ocean. *Ocean Dyn.* 54 (1), 66–76.
- van Vledder, G.P., 2006. The WRT method for the computation of non-linear four-wave interactions in discrete spectral wave models. *Coast. Eng.* 53 (2–3), 223–242.